Andreev Bound States in Topological-Insulator-Based Josephson Junction

by

Yutong Dai

A thesis
presented to the University of Waterloo
in fulfillment of the
thesis requirement for the degree of
Master of Applied Science
in
Electrical & Computer Engineering
(Quantum Information)

Waterloo, Ontario, Canada, 2019

©Yutong Dai 2019

AUTHOR'S DECLARATION

I hereby declare that I am the sole author of this thesis. This is a true copy of the thesis, including any required final revisions, as accepted by my examiners.

I understand that my thesis may be made electronically available to the public.

Abstract

The discovering and manipulating of Majorana fermions have been the frontier of condensed matter physics, not only because it is the first realization of Majorana's theoretical prediction, but also because of its promising application for topological quantum computation. Several ingenious setups are proposed to provide potential platforms for the detection of Majorana fermions. Among them, the topological insulator (TI) based Josephson junctions has drawn appreciable attentions, considering its advantages to realize large-scale Majorana networks.

The study of this thesis explored the relation between Majorana modes and Andreev bound states in a Josephson junction, by calculating and simulating the energy-phase diagram of Andreev bound states. We demonstrated that although the proximity effect is necessary for engineering Majorana modes, too strong proximity effect in a Josephson junction will open a paring gap inside the middle layer and destroy the chiral Majorana modes. The experimental confirmation of this circumstance was also discussed.

In addition, this thesis also described the experimental approach of fabricating lateral Josephson junctions, including molecular beam epitaxy processing (MBE) and nanofabrication processing. To optimize the quality of TI film, the deposition conditions and elementary ratios were investigated by Rheed, XRD and XPS. By depositing superconductive Nb layer on topological insulator and proceeding to nanofabrication, we also achieved the lateral TI based Josephson junctions. The fabrication details were also presented

Acknowledgement

I would like to acknowledge my supervisor Professor Guoxing Miao, who provide continuous support during these years. I would also like to thank Professor Na Young Kim and Professor Adam Tsen for their serves on my thesis committee.

Table of Content

AUTHOR'S DECLARATION....ii
Abstract....iii
Acknowledgement....iv
List of Figures....vi
List of Tables....viii
Chapter1 Introduction....1
1.1Intorduction....1
1.2Thesis outline....3
Chapter2 Background....5
2.1Topological quantum computation....5
2.2Majorana fermions....7
2.3Andreev bound states and fractional Josephson effect....11
Chapter3 Andreev bound states in strong proximity effects....14
3.1Background....14
3.2The TS-TS-TS junction....14
3.2.1Eigenstaets....14
3.2.2Energy-phase diagram of 1D TS-TI-TS junction....17
3.2.3Energy-phase diagram of 2D TS-TI-TS junction....18
Chapter4 Experimental methodology....21
4.1Introduction....21
4.2Molecular Beam Epitaxy (MBE) 21
4.2.1Topological insulator $(Bi_{1-x}Sb_x)_2Te_3$....21
4.2.2MBE system....23
4.2.3Rheed....24
4.2.4X-ray photoelectron spectroscopy (XPS) 25
4.2.5X-ray diffraction (XRD) 25
4.2.6Substrate preparation....26
4.2.7Deposition of topological insulator....27
4.2.8Depostion of superconductive Nb....32
Chapter5 Nanofabrication processing....34
5.1Introduction....34
5.2Optical lithography....34
5.3Reactive ion etching (RIE) for device isolation....37
5.4Electon beam lithography (EBL) 40
5.5RIE for Josephson junction....42
5.6Fabrication results....43
Chapter6 Summary....47
Bibliography....49

List of Figures

Figure 2-1: Illustration of braiding of two particles, and braiding relations..7

Figure2-2: (a)Schematic of edge states in 2D topological insulator. (b) Edge-state dispersion (c) proximate s-wave superconductor drives. (d)Topological phase diagram with Zeeman field is present (e) ferromagnetic insulator, (f) Zeeman field combined with electrostatic gating..8

Figure2-3: Experimental setup for fractional Josephson effect..12

Figure3-1: Reflection coefficients at the interface of two topological superconductors regions...17

Figure3-2: Energy-phase diagram for 1D TS-TS-TS junction...18

Figure3-3: Energy-phase diagram for 2D TS-TS-TS junction...19

Figure 4-1: Josephson Junction fabrication workflow...21

Figure4-2: (a) Crystal structure of $(Bi/Sb)_2Te_3$. (b) Schematic electronic band structure of pure Bi_2Te_3 and pure Sb_2Te_3..22

Figure4-3: Configuration of MBE system...23

Figure4-4: 3D illustration for RHEED..24

Figure4-5: Deposition rate of Bi/Sb/Te..28

Figure4-6: (a-d) Rheed pattern for STO (111) and $(Bi_{1-x}Sb_x)_2Te_3$ (e)Intensity oscillation of RHEED..29

Figure4-7: XRD coupled θ-2θ scan showing peaks from (Bi1-xSbx)2Te3 {0 0 0 1} plane family...30.

Figure 4-8: XPS measurement with Al – Kα 1486 eV source...31

Figure 5-1: MLA 150 UV Maskless Aligner..35

Figure 5-2: Observation of optical lithography results...36

Figure 5-3: Configuration of Oxford PlasmaLab 100 ICP380 Chlorine RIE system..........................38

Figure5-4 (a) RIE parameters for Argon ions recipe. (b) The burned resist on a wafer. (c) A well-etched wafer...39

Figure 5-5: The JBX-6300FS tools..41

Figure 5-6: Device isolation results. Observed by microscope. (a)Device isolation result by EBL does 220UC/cm2 (b) Overdoes situation of EBL..42

Figure 5-7: Software interface of RIE system. (a) Etching time of SF6 recipe. Measured by laser end. (b) Parameter settings of RIE recipe for Junction etching...42

Figure 5-8: JSM 7200-F SEM 43

Figure 5-9: (a&b) SEM picture of Josephson Junction. Re-deposition will result in an extra channel. (white line connecting two superconducting regions.) (c) The width of junction is 138.5nm...44

Figure 5-10: SEM picture demonstrating re-deposition problem..45

List of Tables

Table5-1: Atomic weights of different area in Josephson junction by EDX analysis...........................45

Chapter 1

Introduction

1.1 Introduction

During the last decade, quantum computation was rapidly developed. However, the decoherence remains a huge challenge, because the coupling between qubits and the environment will destroy the entanglement, which is the basic source for quantum computation. Kitaev [1] has proposed a topological quantum computation scheme based on Majorana fermions. Due to its non-locality, topological quantum computing is naturally immune to the local perturbation caused from the coupling between the environment and qubits. [2,3]

At the time, discovering Majorana fermions has become a frontier of condensed matter physics. Several setups for detecting Majorana fermions are proposed based on the theoretical work of Professor Fu and Kane [4,5], where they have demonstrated the existence of Majorana fermions in a tri-junction structure of Josephson junction. This scheme aims to discover Majorana fermions in tri-junction structure, and then exploiting proximity effect to manipulate Majorana fermions. Based on these works, experiments will finally fabricate Majorana fermions network, which is capable of demonstrating basic quantum computation algorithm. This will be a significant progress on the way to topological quantum computation.

To realize Majorana fermions in a Kiteav chain [1,6], the edge states of topological insulator with superconducting proximity effect is engineered. By adjusting the chemical potential and applying magnetic field, Majorana fermions will appear at the interface between topological phase and trivial phase in a Josephson junction. Their existence can be confirmed by the observation of 4π periodic states in the Shapiro measurement.[7]

Although numerous works have analyzed the lateral Josephson junctions,[8] the vertical junction has not been investigated. Considering the fact that the thickness of the middle layer is smaller than the superconducting coherence length, we proposed that the middle layer would be influenced by

the proximity effect. Then, we demonstrated that despite the necessity of proximity effect to discover Majorana fermions, too strong proximity effect will completely make Majorana fermions vanish by opening a gap inside the middle layer. At the same time, we also fabricated Josephson junction with molecular beam epitaxy and nanofabrication methods and observed the fabrication by SEM. The difficulties to fabricate TI based Josephson junction and potential improvement were also discussed.

1.2 Thesis outline

The chapters of this thesis are organized as follow:

Chapter 2 briefly reviews the basic concepts of topological quantum computation, Majorana fermions and Andreev bound states. This includes basic concepts and braiding statistics of anyons, and the approach of engineering Majorana fermions at the edge of 2-dimensional topological insulators. The fractional Josephson effect and methods to detect Majorana fermions are also introduced.

Chapter3 starts by introducing the relation of Majorana zero modes and Andreev bound states. Then, the theoretical calculation and simulation of Andreev bound states in topological insulator-based Josephson junction are presented. The simulation results of reflection coefficients and energy-phase diagram are explained. Finally, the influence of strong proximity effect and the experimental demonstration are discussed.

Chapter4 describes the experimental approach for fabricating Josephson junctions, mostly about Molecular Beam Epitaxy (MBE) processing. After briefly reviewing the entire experimental steps in section 4-1, detailed MBE methods are presented in section 4-2, including deposition and characterization tools, material property of the $(Bi_{1-x}Sb_x)_2Te_3$, and the growth of $(Bi_{1-x}Sb_x)_2Te_3$. The XRD and XPS measurements are also included.

Chapter5 focuses on the nanofabrication of Josephson junction. After reviewing the entire nanofabrication processing, the steps for optical lithography, reactive ion etching, and electron beam lithography are described in detail. Then, the SEM picture shows the major parameters of Josephson junctions as fabrication results. Finally, the difficulties to fabricate Josephson junction and demonstration of fractional Josephson effect are discussed.

Chapter6 summarizes the entire research presented in this thesis and proposes potential

improvement for experimental realization of Majorana fermions

Chapter 2

Background

2.1 Topological quantum computation

One of the most important technological development of 20th century is the Information Technology, which is based on the micro-electronic technology and computer science. During last 50 years, the development of micro-electronics can be summarized by the famous Moore's law: the number of transistors in a dense integrated circuit doubles about every two years. [9] However, it has become a common sense that Moore's law will become invalid as the dimension of micro-electronic devices decreases into nano scales, because electrons in devices will disobey classical dynamics and reach quantum regime. Quantum computation can substantially solve this problem.

Quantum computation requires large-scale entangled system with enough lifetime for the operation of quantum algorithms. [10] However, the decoherence problem posts a huge changeling for realizing scalable quantum computation. Recently, topological quantum computation has emerged as the most promising approach for quantum computation because of its instinct immunity to the decoherence caused by the local coupling between the quantum system and the environment. Compared to other approaches, topological quantum computation exploits non-Abelian quantum phases of matter to perform operations that is not possible for classical computers.

The non-Abelian quasiparticles (also known non-Abelian anyons) [11] are referred to the quasiparticles whose quantum statistical properties are not Fermion-like or Boson-like. Quantum statistics arises from the indistinguishability of quantum particles (including elementary excitations in condensed matter), which is of great importance in quantum systems. Suppose N particles in 3+1 dimensions are moved from their initial positions $(R_1, R_2 \ldots, R_N, t_{initial})$ to final positions $(R_1, R_2 \ldots, R_N, t_{final})$. If theses particles are distinguishable, their trajectories can be

deformed smoothly into a case where there is no movement at all. However, it is not possible to tell the different trajectories apart if these particles are indistinguishable, so permutation groups are developed to describe the topological classes of trajectories.

In 2-dimensional systems, the situation is quite different. When a particle travels around another particle, its trajectory cannot be deformed to a point without cutting through another particle. The exchange of two identical particles in 2-dimensional systems will cause a phase change in the wavefunction: $\phi(R_1, R_2) \rightarrow e^{i\theta}\phi(R_1, R_2)$. If $\theta = 0, \text{or } \pi$, the particles are bosons or fermions, respectively. In other cases, the particles are called *anyons*. The phase θ is called statistical angle. Different type of anyons has different statistical angles.[11]

Considering N particles in 2-dimensional systems are moved from initial position $(R_1, R_2 \dots, R_N, t_{initial})$ to final positions $(R_1, R_2 \dots, R_N, t_{final})$, their trajectories form one element of a *braid group*. A braid group can be expressed as a set of strands connecting initial positions and final positions in figure 1. There are three major requirements of a braid group: 1) each line must be a one-to-one mapping from initial positions to final positions. 2) lines must be continuous along timeline. 3) lines cannot double back, because this situation represents annihilation/creation of particles. Usually, σ_i is defined as anti-clockwise exchange of *i* th particle and *i+1* th particle. Then, we have $\sigma_i\sigma_j = \sigma_j\sigma_i, if\ |i-j| \geq 2$ and $\sigma_i\sigma_{i+1}\sigma_i = \sigma_{i+1}\sigma_i\sigma_{+1i}$ (which is shown in figure 1). When N particles are moved from positions $(R_1, R_2 \dots, R_N, t_1)$ to positions $(R_1, R_2 \dots, R_N, t_2)$, and then to positions $(R_1, R_2 \dots, R_N, t_3)$, their worldlines can be simply stacked along time line from t_1 to t_2, and then to t_3. If these permutation operators are not commutable, their multiply order must be the same with stacking order, the anyons are called *non-Abelian anyons*.[10]

Another important feature about anyons is the fusion rules. Two types of anyons can fuse into a new type of anyons as they are close enough. As the quantum numbers are internal quantities, fusion usually provides new quantum numbers together with new type of anyons. The different fusion forms are called *fusion channel*: $\phi_a \times \phi_b = \sum_c N_c^{ab}\phi_c$, where ϕ is statistical angle. A simple model is “Ising model”, where there are three types anyons: $1, \sigma, \text{and } \psi$. Their fusion

rules are: $\sigma \times \sigma = 1 + \psi, \sigma \times \psi = \sigma, \psi \times \psi = 1, \text{and } 1 \times x = x, \text{where } x = 1, \sigma, \text{or } \psi$. In a system with four σ particles, these four particles can be divided into two groups: 1 and 2, 3 and 4. If we constrain these four particles fuse into 1, then 12 must fuse to the same type as 34 do (34 can fuse into $1 \text{ or } \psi$). These states Ψ_1 *and* Ψ_ψ will form the basis of Hilbert space of 4 particles, which can be encoded as 0 and 1 in a qubit.

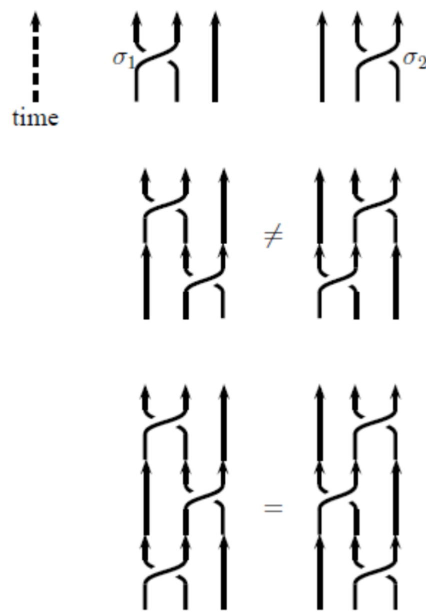

Figure 2-1: Illustration of braiding of two particles, and braiding relations. [10]

2.2 Majorana Fermions

70 years ago, Ettore Majorana proposed a new elementary particle known as "Majorana Fermions", which constitute their own antiparticles [6]. Despite its long history, the observation of Majorana Fermions remains an outstanding goal. Unlike high-energy physicists, condensed matter physicists chasing Majorana's vision by exploiting nontrivial emergent excitations. The observation of Majorana Fermions in condensed matter physics constitute a landmark achievement, both because it is the first realization of Ettore Majorana's theoretical predication and, more importantly, because of the non-Abelian statistics that they obey.

Superconductor is a naturally hosting platform for Majorana fermions because of its intrinsic

emergent excitations——Cooper pairs. However, the electrons of a common s-wave Cooper pair have opposite spins, which leads to the difference of quasiparticles operators and its antiparticle counterpart. This difference violates the basic requirement of Majorana fermions, that they are their own antiparticles. Therefore, the 'spinless' p-wave superconductor become the candidate for searching of Majorana fermions, because only one spin freedom is active in p-wave superconductors. To overcome the rareness of p-wave superconductor, several ingenious schemes that exploits proximity effect of s-wave superconductor and topological insulator to realize Majorana fermions are proposed.

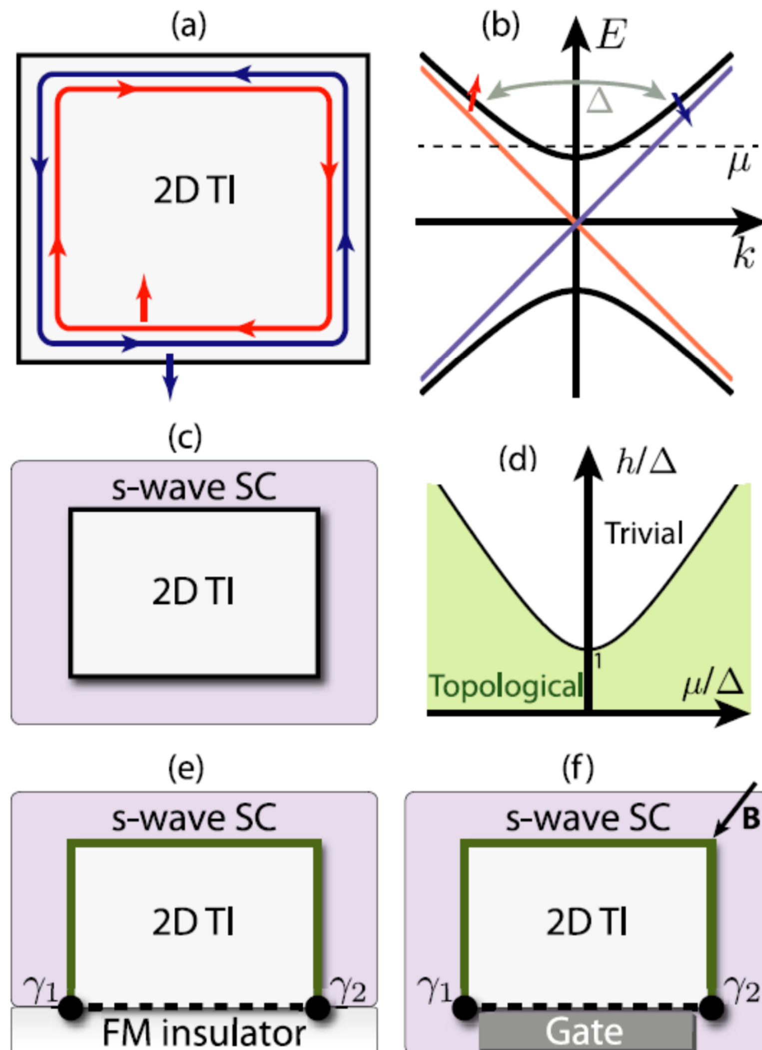

Figure 2-2: (a)Schemes of counter-propagating, spin-filtered edge states in a 2D topological

insulator. (b) Energy dispersion of edge states when time-reversal symmetry is present (red and blue lines). Zeeman field h will open a gap (solid curves). (c) The proximity effect from s-wave superconductor drives the edge into a topological phase similar to the weak-pairing phase in Kitaev's toy model for a 1D spinless p-wave superconductor. When the Zeeman field h is present, the topological phase survives provided $\mathrm{h} < \sqrt{\mu^2 + \Delta^2}$, leading to the phase diagram in (d). Domain walls between topological (green lines) and trivial regions (dashed lines) on the edge trap localized Majorana zero-modes. These can be created with (e) a ferromagnetic insulator, (f) a Zeeman field combined with electrostatic gating. [6]

Figure 2-2 (c) is one basic setup for pursuit of Majorana fermions, where the counter-propagating edge states of 2D topological insulator are gapped out by the proximity-effect-induced superconductivity. For simplification, the edge states of 2D topological insulator can be described as two counter-propagating low energy states, with opposite spin directions (Figure (a)). These states are connected to each other by time-reversal symmetry, and their Hamiltonian is

$$H_{2DTI} = \int dx\, \phi^{+}(-iv\partial_x \sigma^x - \mu)\phi$$

where ν is the fermion velocity, μ is the chemical potential, and $\phi^{+}_{\sigma x}$ creates one electron with spin σ and position x in the edge states. Their dispersion relations are depicted in Figure (b). The red (blue) line is corresponding to the clockwise (contraclockwise) edge state. If the time reversal symmetry is preserved, backscattering between counterpropagating states is impossible due to the lack of scattered state. [12] Therefore, the edge states are robust against non-magnetic defects. At the same time, since there are only one single pair of states supported, the system will circumvent the fermion doubling problem and is effectively considered as "spinless". [13]

When placed adjacent to the s-wave superconductor, the edge states will inherit a superconducting pairing potential due to the proximity effect. The 1D system can be described by the Hamiltonian:

$$\mathrm{H} = H_{2DTI} + H_{\Delta}$$

$$H_{\Delta} = \int dx \Delta(\phi_{\uparrow}\phi_{\downarrow} + H.c.)$$

where Δ is the pairing potential of 1D edge states.[14] The energy dispersion can be derived from the Hamiltonian:

$$\mathrm{E} = \sqrt{(\pm vk - \mu)^2 + \Delta^2}$$

where k is the momentum. This topological superconductor is corresponding to the weak-paring phase of Kitaev chain model.

As in 1D Kitaev chain, Majorana bond states will appear at the interface of topological phase (weak-paring phase) and trivial phase. It is intuitive to induce part of the chain into trivial phase by breaking the time reversal symmetry with an applied magnetic field. The magnetic field will introduce a Zeeman tern into the origin Hamiltonian:[15]

$$\mathrm{H} = H_{2DTI} + H_{\Delta} + H_{z}$$

$$H_{Z} = -h \int dx\, \phi^{+} \sigma_x \phi$$

where H_Z is the Zeeman split induced by magnetic ferromagnetic insulator with $\mathrm{h} \geq 0$. (as in Figure2-2 (e)) If there is no paring potential ($\Delta = 0$), the energy dispersion $\mathrm{E}_{\pm}(\mathrm{k}) = -\mu \pm \sqrt{(vk)^2 + \Delta^2}$ is shown as the solid line in Figure (b). The breaking of time reversal symmetry results in an energy gap at k=0 point. Adjusting the chemical potential μ near the bottom of conductive band as the dashed line in Figure (b), can lead to the effective p-wave paring because the wavefunction of the valence band can be neglected. Thus, after expanding the energy $\epsilon_{+}(k) \approx -(\mu - h) + \frac{v^2}{2h} k^2 = -\mu_{eff} + \frac{k^2}{2m_{eff}}$, the Hamiltonian can be described as:

$$H_{eff} = \int dx \left[\phi_{+}^{+} \left(-\frac{\partial_x^2}{2m_{eff}} - \mu_{eff} \right) \phi_{+} + \frac{\Delta_{eff}}{2} (-\phi_{+} i \partial_x \phi_{+} + H.c.) \right]$$

where ϕ_{+} is the wavefunction of conductive band. At the same time, the magnetic filed has to be strong enough $\mathrm{h} \gg \Delta$, to make sure the edge states are within the strong painting phase. (Figure2-2 (d))[16]

Figure 2-2 (e) and (f) show two setups realizing Majorana fermions at the end of a topological

phase chain. The topological phase chains are shown as the green lines formed by gapping out the edge states of 2D topological insulator with proximity effect of adjacent superconductor, while the dashed line is the trivial phase formed by introducing Zeeman filed. [17] In (e), the proximity effect of a ferromagnetic insulator induces a Zeeman field on the edge state (dashed line). In (f), the magnetic field is applied uniformly through the setup so that all four edges are influenced by the Zeeman filed. In this case, the topological phase and trivial phase are simply distinguished by applying a gate voltage that changes the chemical potential of the fourth edge.[18]

2.3 Andreev bound states and fractional Josephson effect

In 2008, Fu and Kane [4] proposed the approach for creating and manipulating Majorana fermions in a topological-insulator-based Josephson junction. Compared to 1D semiconductor nano-wire setups, the manipulation of Majorana fermions in Josephson junction can be simply realized by adjusting the superconductor phase, which provide a potential solution to large-scale quantum circuits. Since then, creating and detecting Majorana bound states in Josephson junction has been the goal for many experimental groups.

As predicted by Fu and Kane [4], Majorana bound states would appear at the interface of a topological superconductor and a topological insulator. In this unconventional Josephson junction, the interaction of two Majorana fermions (γ_1 and γ_2 in Figure 2-3)) will render a tunneling effect and cause the so-called fractional Josephson effect. [19] The Hamiltonian of this system can be described as:

$$\mathrm{H} = \sum_{i=L/R} H_i + H_T$$

$$H_i = -\frac{t}{2}\sum_{i=1}^{i=N-1} c_{ix}^{+}c_{ix+1}^{+} + e^{i\phi_i}c_{ix}c_{ix+1} + h.c$$

$$H_T = -\Gamma(c_{LN}^{+}c_{R1} + H.c.)$$

where H_i is the Hamiltonian of the Kitaev chain (green line in Figure 2-3), and H_T is the

tunneling effect of two Majorana fermions. After projecting the Hamiltonian into the zero-energy subspace, [20] we can recombine two Majorana operators if two Majorana mode overlap appreciably, which yields:

$$\begin{aligned} H' &= -\frac{\Gamma}{2}\cos\left(\frac{\Delta\phi}{2}\right) i\gamma_1\gamma_2 \\ &= -\Gamma\cos\left(\frac{\Delta\phi}{2}\right)(n_1 - \frac{1}{2}) \end{aligned}$$

where $\Delta\phi$ is the phase difference of two superconductor regions.[21] Usually, n_1 is conserved by the fermion parity. The current across the Josephson junction can be obtain by: [22]

$$I = \frac{2e}{\hbar}\frac{\partial\langle H'\rangle}{\partial\Delta\phi} = \frac{e\Gamma}{2\hbar}\sin\left(\frac{\Delta\phi}{2}\right)(2n_1 - 1)$$

This current exhibit the significant difference with traditional Josephson current——4-pi periodicity.

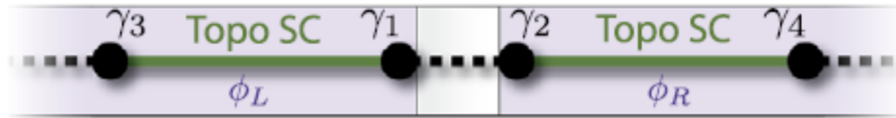

Figure 2-3: Basic experimental setup required to observe the fractional Josephson effect stemming from Majorana modes [6]

The Josephson current derived above is the so-called *fractional Josephson effect*. Compared to traditional Josephson effect, only "half" of the cooper pair tunnels across the junction, so the amplitude of supercurrent is only half of traditional Josephson current. [24] For conventional Josephson junction, because of the superconducting gap, single electron tunneling is suppressed, while in fractional Josephson effect, the coupling between two Majorana modes makes single electron tunneling possible. Therefore, fractional Josephson effect has a smaller amplitude.

Another important feature of fractional Josephson effect is the 4π periodicity of energy-phase relation. [25,26] Although the Hamiltonian is 2π periodic, the states has 4π periodicity. After sweeping phase difference from 0 to 2π, the states acquire a minus sign and only after advancing anther 2π, the states will return back. This 4π periodicity is never discovered in traditional Josephson effect, which makes it the most convincing evidence for discovering Majorana

fermions in a Josephson junction. Experimentally, two major issues have to be solved in order to observe 4π periodic states. First, it is necessary to separate 4π states from 2π states. For a current-voltage measurement, the 2π periodic current contributed by traditional Josephson effect may obscure 4π current signal. Fortunately, in the Shapiro measurement of a current-bias Josephson junction, it is demonstrated that the 4π current has larger amplitude than 2π current when the ac signal is in relatively low frequency.[27] Second, the hybridization of outer Majorana modes will open gaps at crossing points in energy-phase diagram, which will cause the disappearance of 4π periodic current. This can be circumvented by enlarging the topological phase, and the gap will decay with the length exponentially. [28]

Chapter 3

Andreev bound states in strong proximity effects

3.1. Background

The conceptual breakthrough for engineering Majorana fermions originated with the seminal work of Fu and Kane in the context of topological insulators. [4,6] They proposed that Majorana states can in principle be engineered and manipulated by using junctions of superconductors on the surface of a topological insulator. Based on their works, other groups also investigated topological-insulator-based Josephson junctions, [8] from the energy-phase dispersion of the Andreev bound state, the appearance of 4-pi periodic states as the evidence of Majorana bound states, to the influence of different chemical potentials. Here, we investigated the vertical Josephson junction formed by a topological insulator sandwiched by two superconductor region and proposed that a topological superconducting region is induced in the middle due to the proximity effect. The induced paring potential in topological superconductor region will open a gap at Fermin surface, and the 4-π periodic Andreev bound states disappears in these circumstances. We then generalize the analysis to a 2D junction and calculated the energy-phase diagram of Andreev bound states at different incident angles. In this case we found that the 4-π periodic Andreev only exists at zero incident angle when induced paring potential is also zero. Finally, we concluded that in contrary to the benefits of proximity effect, too strong proximity effect will introduce a gap in the topological insulator region, dismiss 4-pi periodic Andreev bound states and cause the extinction of Majorana bound states.

3.2. The TS—TS—TS Junction

3.2.1 Eigenstates

In the vertical Josephson Junction, because the thickness of topological insulator region is less

than the correlation length of superconductor, we assume that a uniform paring potential is formed by proximity effect and the topological insulator region is replaced by a topological superconductor (TS) region. In the Nambu basis $\Psi = (\psi_\uparrow, \psi_\downarrow, \psi_\uparrow^+, \psi_\downarrow^+)^T$, the Hamiltonian of TS region can be expressed as:

$$\mathrm{H}_{TS} = \begin{pmatrix} H_0(\vec{k}) & \Delta(\vec{k}) \\ -\Delta^*(\vec{k}) & -H_0^*(\vec{k}) \end{pmatrix} = \begin{pmatrix} -\mu & \nu_F k_x - i\nu_F k_y & 0 & \Delta e^{i\phi} \\ \nu_F k_x + i\nu_F k_y & -\mu & -\Delta e^{i\phi} & 0 \\ 0 & -\Delta e^{-i\phi} & \mu & \nu_F k_x + i\nu_F k_y \\ \Delta e^{-i\phi} & 0 & \nu_F k_x - i\nu_F k_y & \mu \end{pmatrix}$$

where Δ is the paring potential inherited from superconductor by proximity effect. And $\Delta = \begin{pmatrix} 0 & \Delta e^{i\phi} \\ -\Delta e^{i\phi} & 0 \end{pmatrix}$ describes a s-wave superconductor. Based on the Hamiltonian, we can derive the eigenstates of topological superconductor region are:

$$\Psi_{TS,e} = \frac{1}{2\sqrt{\epsilon}} e^{ik_x' x + ik_y y}\left[e^{i\phi_{Ts}}\sqrt{\epsilon - \mu + |k|}, e^{i\phi_s} e^{i\theta}\sqrt{\epsilon - \mu + |k|}, -\frac{\Delta e^{i\theta}}{\sqrt{\epsilon - \mu + |k|}}, \frac{\Delta}{\sqrt{\epsilon - \mu + |k|}}\right]$$

$$\Psi_{TS,h} = \frac{1}{2\sqrt{\epsilon}} e^{-ik_x' x + ik_y y}\left[e^{i\phi_{Ts}}\sqrt{\epsilon - \mu + |k|}, -e^{i\phi_s} e^{-i\theta}\sqrt{\epsilon - \mu + |k|}, \frac{\Delta e^{-i\theta}}{\sqrt{\epsilon - \mu + |k|}}, \frac{\Delta}{\sqrt{\epsilon - \mu + |k|}}\right]$$

We assume that in the TS—TS—TS junction, the paring potentials in the middle layer has different amplitude:

$$\Delta(\vec{k}) = \begin{cases} \Delta_R i\sigma_y e^{i\phi_R} & x > \frac{L}{2} \\ \Delta_M i\sigma_y e^{i\phi_M} & \frac{L}{2} > x > -\frac{L}{2} \\ \Delta_L i\sigma_y e^{i\phi_L,} & x < -\frac{L}{2} \end{cases}$$

For small junction limit, the phase difference is assumed to be $\phi_M - \phi_L = 0$, and $\phi_R - \phi_M = \Phi$, and paring potentials are $\Delta_L = \Delta_R > \Delta_M$

The reelection and transmission coefficients are different at both interfaces. But we can calculate the normal and Andreev reflection coefficients by making wave function continuous. For example, at the right interface, the incoming electrons can be reflected as electrons (normal reflection) or as holes (Andreev reflection):

$$\Psi_{Middle,e\rightarrow} + r_{ee}\Psi_{Middle,e\leftarrow} + r_{eh}\Psi_{Middle,h\leftarrow} = t_{ee}\Psi_{Right,e\rightarrow} + t_{eh}\Psi_{Right,h\rightarrow}$$

which is:

$$\frac{1}{2\sqrt{\epsilon}}\begin{pmatrix} e^{i\phi_M} c_M \\ e^{i\phi_M} e^{i\theta_M} c_M \\ -\Delta_M e^{i\theta_M}/c_M \\ \Delta_M/c_M \end{pmatrix} + \frac{r_{ee}}{2\sqrt{\epsilon}}\begin{pmatrix} e^{i\phi_M} c_M \\ -e^{i\phi_M} e^{-i\theta_M} c_M \\ \Delta_M e^{-i\theta_M}/c_M \\ \Delta_M/c_M \end{pmatrix} + \frac{r_{eh}}{2\sqrt{\epsilon}}\begin{pmatrix} e^{i\phi_M} d_M \\ e^{i\phi_M} e^{i\theta_M} d_M \\ -\Delta_M e^{i\theta_M}/d_M \\ \Delta_M/d_M \end{pmatrix}$$

$$= \frac{t_{ee}}{\sqrt{2}\sqrt{\epsilon}}\begin{pmatrix} e^{i\phi_R} c_R \\ e^{i\phi_R} e^{i\theta_R} c_R \\ -\Delta_R e^{i\theta_R}/c_R \\ \Delta_R/c_R \end{pmatrix} + \frac{t_{eh}}{\sqrt{2}\sqrt{\epsilon}}\begin{pmatrix} e^{i\phi_R} c_R \\ -e^{i\phi_R} e^{-i\theta_R} c_R \\ \Delta_R e^{-i\theta_R}/c_R \\ \Delta_R/c_R \end{pmatrix}$$

Where, c and d are defined as:

$c_{M\backslash R}=\sqrt{\epsilon-\mu_{M\backslash R}+v|k_{e,M\backslash R}|}$ and $d_{M\backslash R}=\sqrt{\epsilon-\mu_{M\backslash R}+v|k_{h,M\backslash R}|}$

$$k_{e,M\backslash R}=\mu_{M\backslash R}/v+\sqrt{\epsilon^2-\Delta_{M\backslash R}^2}$$

$$k_{h,M\backslash R}=\mu_{M\backslash R}/v-\sqrt{\epsilon^2-\Delta_{M\backslash R}^2}$$

$\theta_{M\backslash R}$ is the incident angle, where zero angle means orthogonal to the interface. The relationship between θ_M and θ_R is determined by the conservation of $k_{\parallel}$, which is $\theta_R=\arcsin(sin\theta_M\mu_M/\mu_R)$.

In order to simplify the calculation, we define some parameters:

$$X_1=\frac{e^{-i\theta_R}-e^{-i\theta_M}}{e^{-i\theta_R}+e^{i\theta_M}}, and\ X_2=\frac{e^{i\theta_R}+e^{-i\theta_M}}{e^{i\theta_R}-e^{i\theta_M}}$$

$$D_1=\frac{\Delta_M c_R^2 e^{i\phi}}{\Delta_R}, \text{and } D_2=\frac{\Delta_M d_R^2 e^{i\phi}}{\Delta_R}$$

Then, we have

$$r_{ee,r}=-\frac{\left(c_M-\frac{D_1}{c_M}\right)\left(d_M-\frac{D_2}{d_M}\right)-\left(c_M-\frac{D_2}{c_M}\right)\left(d_M-\frac{D_1}{d_M}\right)}{X_1\left(c_M-\frac{D_1}{c_M}\right)\left(d_M-\frac{D_2}{d_M}\right)-X_2\left(c_M-\frac{D_2}{c_M}\right)\left(d_M-\frac{D_1}{d_M}\right)}$$

$$r_{eh,r}=-\frac{(X_1-X_2)\left(c_M-\frac{D_1}{c_M}\right)\left(c_M-\frac{D_2}{c_M}\right)}{X_1\left(c_M-\frac{D_1}{c_M}\right)\left(d_M-\frac{D_2}{d_M}\right)-X_2\left(c_M-\frac{D_2}{c_M}\right)\left(d_M-\frac{D_1}{d_M}\right)}$$

Reflection coefficients at left interface can be calculated similarly. For a 1D junction, it is effective to assume that incident angles are all zero.

Figure 2 are the simulation results of normal reflection coefficient r_{ee} (red line) and Andreev reflection confident r_{eh} (green line). At zero incident angle, the incoming electrons are all reflected as holes (Andreev reflection) However, at the glancing incident angle, the Andreev reflection is suppressed and the amplitude for normal reflection is almost one. At other incident angles, electrons with higher energy are more likely to undergo Andreev reflection.

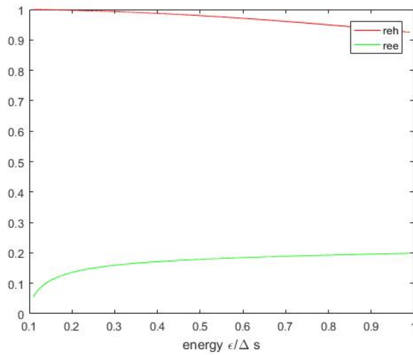

(a)

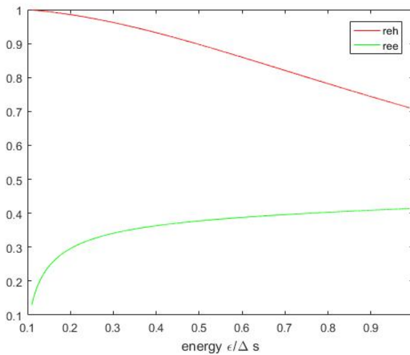

(b)

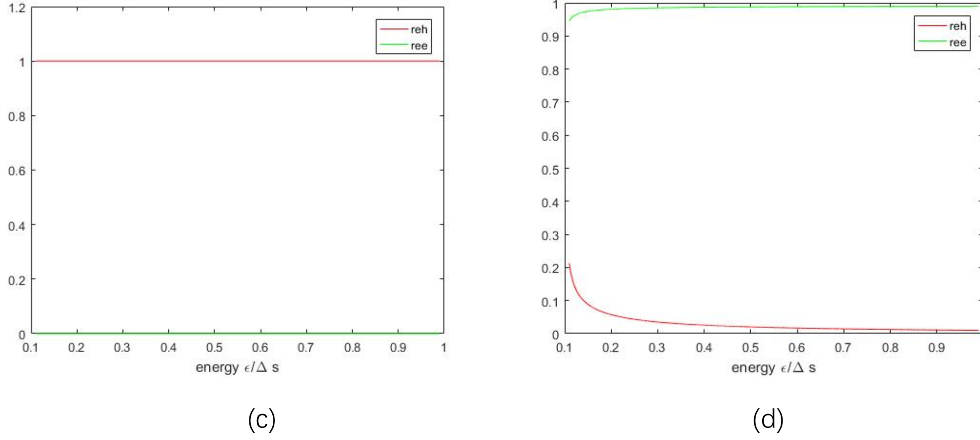

(c) (d)

Figure3-1: Reflection coefficients. Red line is reh, and green line is ree. Phase difference is pi. S region, $\Delta_S = 1$, TS region, $\Delta_{TS} = 0.1\Delta_s$. energy range: $\epsilon \sim 0.11 - 0.99$,. incident angle (a) π/8 (b)π/4 (c)0 (d)π/2.

Continuity equations: the incident electrons are reflected as holes, and vice versa. Therefore, there should be quantized Andreev bound states. The solutions of Bogoliubov-de Gennes equations should be:

$$\Psi(\mathrm{x}, \mathrm{E}) = a\Psi_e^+(x, E) + b\Psi_h^+(x, E) + c\Psi_e^-(x, E) + d\Psi_h^-(x, E)$$

To calculate the energy of bound states, we need to solve continuity equations:

$$ce^{-i|k_e|l} = r_{ee,r}\mathrm{a}e^{i|k_e|l} + r_{he,r}de^{-i|k_h|l}$$
$$be^{i|k_h|l} = r_{eh,r}\mathrm{a}e^{i|k_e|l} + r_{hh,r}de^{-i|k_h|l}$$
$$\mathrm{a}e^{-i|k_e|l} = r_{ee,l}ce^{i|k_e|l} + r_{he,l}be^{-i|k_h|l}$$
$$de^{i|k_h|l} = r_{eh,l}ce^{i|k_e|l} + r_{hh,l}be^{-i|k_h|l}$$

Where $k_e = \mu_M/v + \sqrt{\epsilon^2 - \Delta_M^2}$ and $k_h = \mu_M/v - \sqrt{\epsilon^2 - \Delta_M^2}$.

3.2.2 Energy-phase diagram of 1D TS-TI-TS junction

By solving continuity equations in section 3.2.2, we obtain the energy-phase diagram of a 1D junction. This special can approached by simply setting incident angles and paring potential of middle layer to zero. Here, we assume that $\mu_M = 100 * \Delta_R$ and $\mu_R = 1000 * \Delta_R$. We demonstrate that even for such high electron density. The 4-pi periodic state is present. We also assume that the junction length is much smaller than the coherence length of superconductor ($\mathrm{L}/L_0 = 0.001$, where $L_0 = v_f\hbar/\mu_{TS}$). In this case, it is valid to assume the phase is changing linearly inside the junction. The phase of the middle point of the junction is set to 0, while the phase of left superconductor is $-\phi$, and right one is $+\phi$. Then, we show that there is at least one bound state for each spin.

Figure3-2 is the energy-phase diagram of a 1D Josephson junction. The red and blue lines indicate the opposite spin direction. The crossing at π and 3π points are protected by Fermion parity. Therefore, when advancing phase difference from 0 to 4-pi, each branch follows its own

path and exhibit a clear 4-pi periodicity. When the phase difference of two superconductor region is π , there exist a zero-energy mode with a dispersion of k_y. This is known as the nonchiral Majorana mode. Furthermore, the existence of these states can be demonstrated by a Shapiro measurement without odd steps.

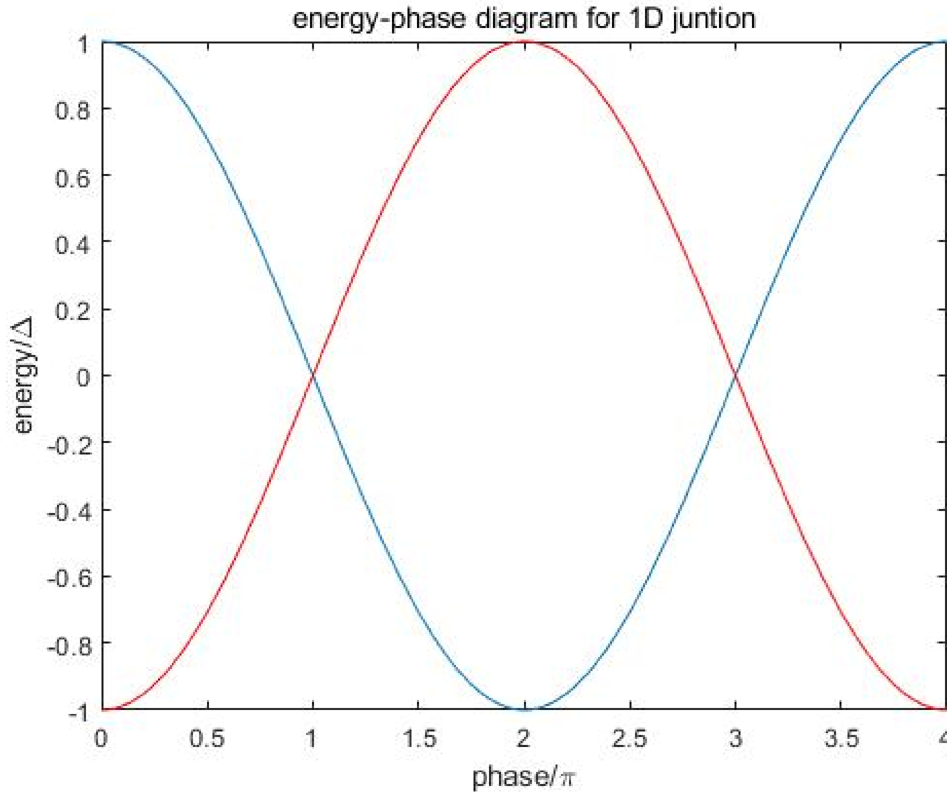

Figure3-2: Energy-phase diagram for 1D TS-TS-TS junction

3.2.3 Energy-phase diagram of 2D TS-TI-TS junction

The situation is complicated for a 2D junction, because of the mismatch of momentum caused by the difference of chemical potential. Electrons with incident angle θ_L is scattered through the channel defined by relation $\theta_R = \arcsin\left(sin\theta_M \mu_M / \mu_R\right)$. Therefore, different scattering channel has different energy-phase relation. To numerically solve the continuity equations, we made a loop over energy and calculated how much the equations deviated for every energy. The numerical results are plotted in Figure .

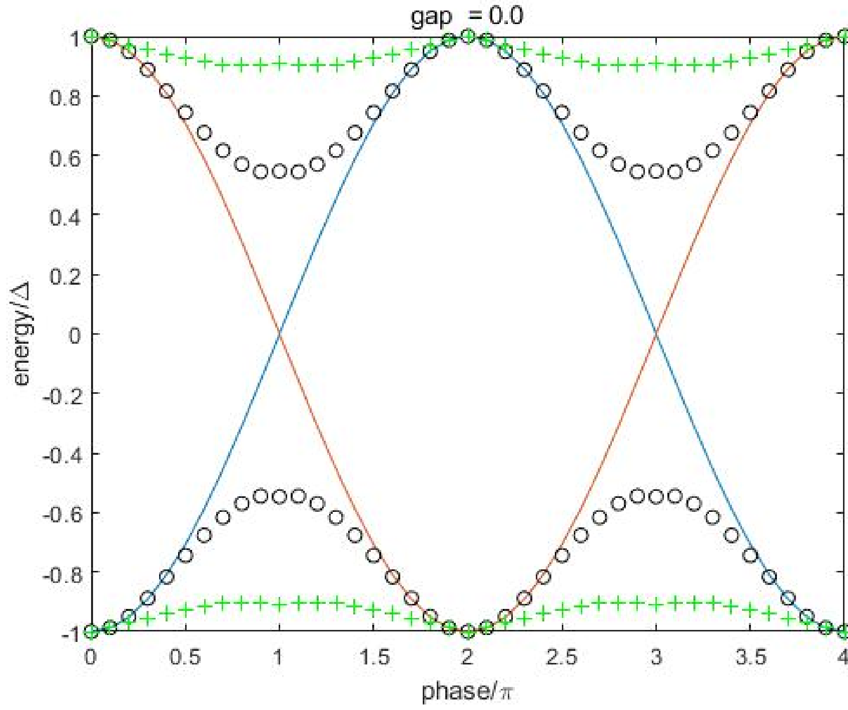

(a)

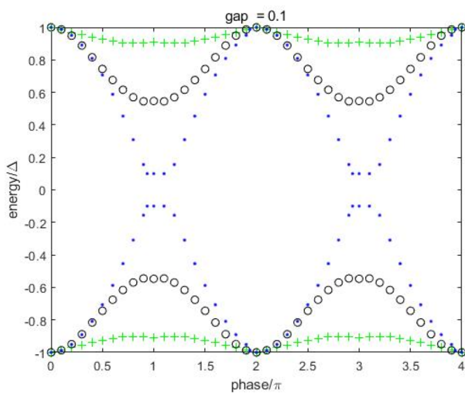

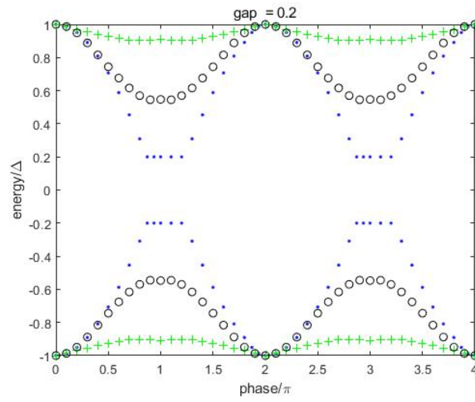

(b) (c)

Figure3-3: Figure3-2: Energy-phase diagram for 2D TS-TS-TS junction (a) Andreev bound states for different trajectories in a TS-TS-TS junction. The middle TS pairing potential is $\Delta_M = 0.0$. The incident angle is $\theta = 0$, for solid blue and red lines. $\theta = 0.2\pi$ for black circle and 0.4π for green plus sign. (b) $\Delta_M = 0.1$ The incident angle is $\theta = 0$, for blue dots. $\theta = 0.2\pi$ for black circle and 0.4π for green plus sign. (c) $\Delta_M = 0.2$ The incident angle is $\theta = 0$, for blue dots. $\theta = 0.2\pi$ for black circle and 0.4π for green plus sign. $\mu_M = 100 * \Delta_R$ and $\mu_R = 1000 * \Delta_R$. For small junctions, $L/L_0 = 0.001$, where $L_0 = v_f\hbar/\mu_{TS}$.

In Figure (a), the paring potential in the middle layer is set to zero. This is the case for TS-TI-TS junction. The 4π periodic bound states (Figure (a) blue and orange lines) only appear at zero incident angle. For non-zero incident angles, an energy gap would exist at zero energy, which change the periodicity to 2π. If the proximity effect is strong enough or the middle layer is thin enough to induce a pairing potential in the middle layer, the energy-phase diagram will be changed drastically near zero energy. For energy lower than the paring potential Δ_M in the middle layer, no bound states can exit inside the junction. For energy higher than Δ_M, the original energy-phase diagram will be truncated at Δ_M and leave an energy gap beside zero energy. Since there are no bound states at zero energy, we conclude that this pairing potential Δ_M would destroy the Majorana bound states, which means Majorana bound states cannot survive in a junction with strong proximity effect.

Chapter 4

Experimental methodology

4.1 Introduction

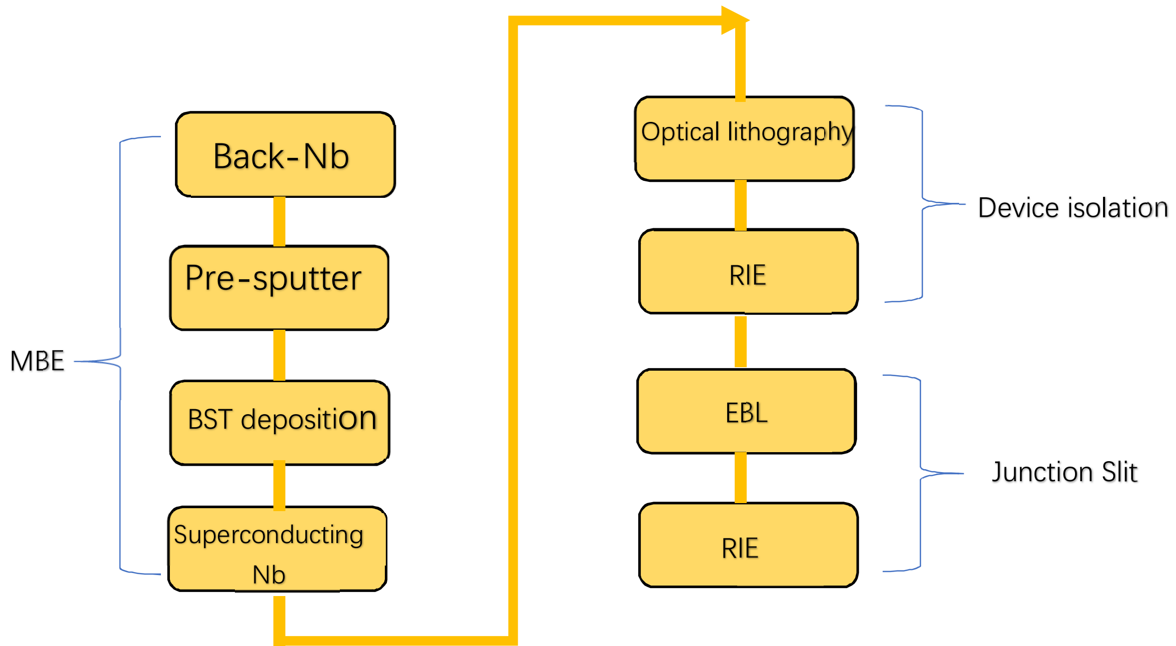

Figure 4-1: Josephson Junction fabrication workflow

The fabrication of Josephson junction has two major steps: the MBE deposition for uniform films, and nanofabrication for devices. In this chapter, I will first review the crystal structure of $(Bi/Sb)_2Te_3$ and the Molecular Beam Epitaxy processing of topological insulator. Then I will review the nanofabrication processing of Josephson junction, which includes the device isolation method and etching method of junction slit. Finally, I will mention the challenge of experimental realization of Majorana modes in Josephson junction.

4.2 Molecular Beam Epitaxy (MBE)

4.2.1 Topological insulator $(Bi_{1-x}Sb_x)_2Te_3$

In 2009, $(Bi, Sb)_2(Se, Te)_3$ family was theoretically demonstrated to be topological insulator, with topologically protected surface states. [29] Then, it is demonstrated that the surface state consists of a single nondegenerate Dirac cone by angle-resolved photoemission spectroscopy. [30,31,32] Compared to selenide topological insulator, telluride topological insulator has instinct advantage because Te has lower vapor pressure which can reduce undesired carriers of bulk states.

Figure (a) shows the rhombohedral crystal structure of $(Bi/Sb)_2Te_3$. Along the [0001] crystal direction, the stacking sequence of Te-Bi/Sb-Te-Bi/Sb-Te, forms a quintuple layer (QL) with one Te atomic layer terminating on both sides. The bond between two atomic layers within a QL is covalent bonding while the interaction between two adjacent QLs is a much weaker van der Waals interaction. [33,34]

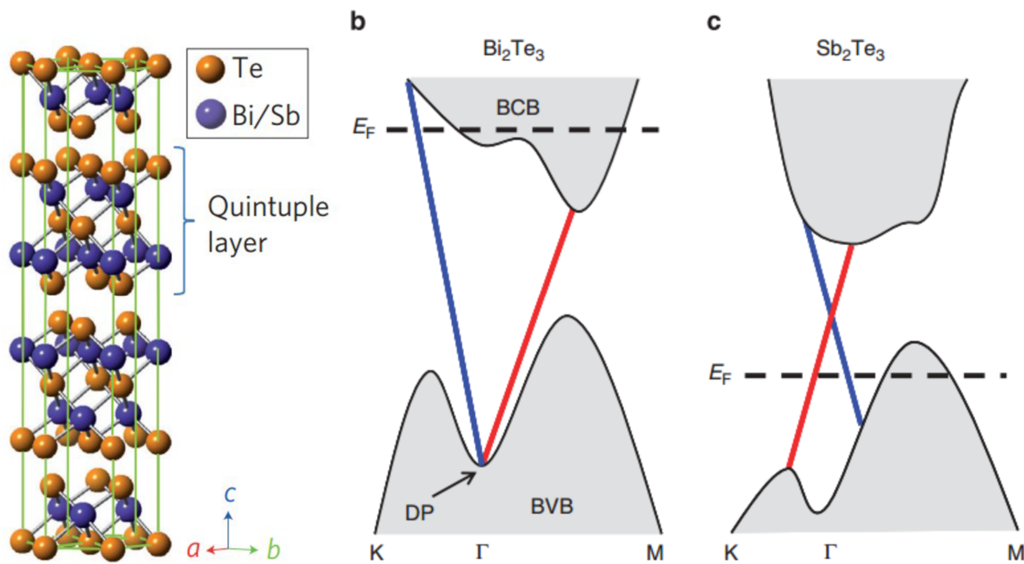

Figure4-2: (a) Crystal structure of (Bi/Sb)2Te3. (b) Schematic electronic band structure of pure Bi2Te3 and pure Sb2Te3. Fermi level in pure Bi2Te3 is buried in conduction band and carriers are n-type. Fermi level in pure Sb2Te3 is buried in valence band and carriers are p-type.[33]

In order to engineering the surface states of telluride topological insulator, the Dirac point is needed to adjust into the band gap of bulk states. This is because the bulk states of $(Bi/Sb)_2Te_3$ is highly metallic and these states would influence the performance of topological surface states.

Another drawback of Bi_2Te_3 is its Dirac point is buried in bulk valence band, which makes it difficult to access the surface state by transport. On the contrary, Sb_2Te_3 has well defined Dirac point in the bulk band gap. Since Bi_2Te_3 and Sb_2Te_3 have the same crystal structure, Bi can be substituted by Sb with arbitrary ratio to form the ternary compound $(Bi_{1-x}Sb_x)_2Te_3$. By mixing Bi and Sb with arbitrary ratio x, the ternary telluride $(Bi_{1-x}Sb_x)_2Te_3$ is also a topological insulator with well-defined Dirac point in the band gap.

4.2.2 MBE system

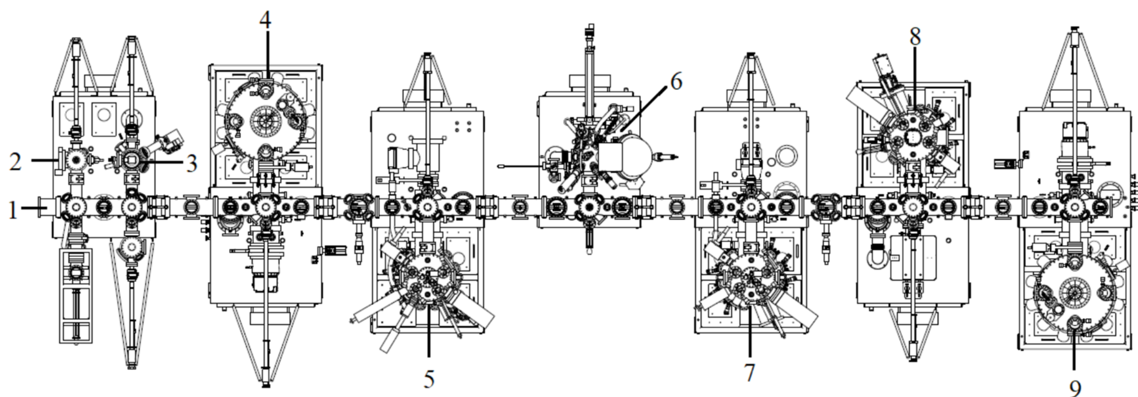

Figure4-3: (1) Vacuum transfer line (2) FEL (3) Sample preparation chamber (4) Magnetron sputtering chamber for superconductors, used to deposit Nb (5) MBE module for TI, used to grow (Bi1-xSbx)2Te3 compound (6) Surface analysis module (7) MBE module for metal oxides (8) MBE and electron beam co-evaporation module

Figure4-3 is the MBE system, consisting of 8 major ultra-high vacuum chambers. The pressure of deposition and analysis chambers is under 10^{-10}mbar and under 10^{-9}mbar. Holders with substrates are loaded by FEL chamber (chamber 2) then transferred into transfer line (module 1) for next steps. Module 3 is the preparation chamber, which is equipped with Argon and Oxygen gas for plasma. Module 6 is the analysis chamber, with XPS and UPS. Chamber 7 is annealing chamber, which is used to anneal sapphire at 1000 degree. Chamber 9 is metal chamber, which is used to deposit magnetic materials. We also have chamber 8 to deposit MgB_2 and sapphire.

Module 5 is used for depositing topological insulator. This module is equipped with three K-cells for Bi and Sb sources and one valved cracker cell for Te sources. High-purity Bi (99.999%) and Sb (99.999%) sources were evaporated by K-cells. Because it is very easy for Te to deposit at the valve of cracker, it is necessary to measure Te deposition rate regularly. [35]

4.2.3 Rheed

Rheed is the most common method to monitor quality of deposited film. The main parts of a RHEED system consist of an electron gun, a fluoresce screen and a CCD camera. Electrons with high energy are injected from electron gun, at glance incident angle to the sample surface. After diffracted by the atomic structure of sample surface, electrons are collected by the fluoresce screen and exhibit the situation of the surface.

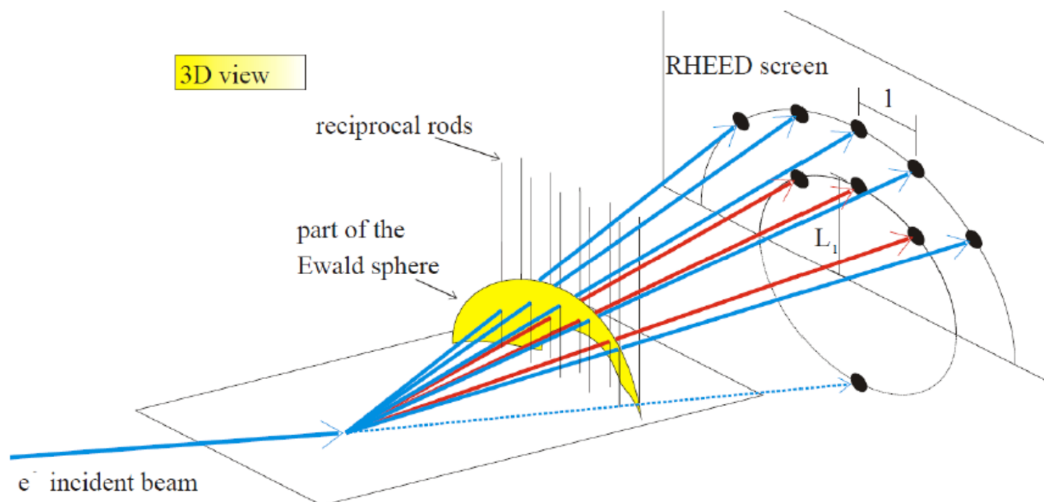

Figure4-4: 3D illustration for RHEED [36]

Although they have high kinetic energy, electrons can only penetrate through 1 nm ~2 nm on the surface of sample, because of the small incident angle. Therefore, Rheed provides information about the surface instead of the bulk. Figure 3-4 illustrates the diffraction principle from a 3D view. [37] Similar to the analysis for diffraction from bulk crystals, the Ewald's sphere is constructed. However, instead of the reciprocal lattice for a 3D material, we will have reciprocal rods transformed from a 2D lattice sheet because only atoms at the sample surface contribute

to the RHEED pattern. A constructive diffraction pattern will form wherever the reciprocal rods intersect the Ewald's sphere, but the screen is setup so that only low orders of diffraction can be detected. By rotating the sample azimuthally, we can get full information about the 2D surface lattice.

4.2.4 X-ray photoelectron spectroscopy (XPS)

XPS is a spectroscopic equipment that is surface-sensitive. It measures the elemental composition at the parts per thousand range, empirical formula, chemical state and electronic state of the elements that exist in the bulk of materials. XPS is a useful measurement technique because it not only shows what elements are within a film but also what other elements they are bonded to.

Our MBE system is equipped with X-ray source (Al – Kα 1486 eV and Mg – Kα 1253 eV), electron source (5000 eV) and ultraviolet photon source (21.4 eV). The analysis chamber is able to do X-ray photoelectron spectroscopy (XPS), auger electron spectroscopy (AES) and ultraviolet photoelectron spectroscopy (UPS). These in-situ characterization methods consist the post-growth measurement module.

4.2.5 X-ray diffraction (XRD)

XRD is used to analyze the crystalline property of thin films and heterostructures. After the growth was fully accomplished and *in-situ* characterizations were done, sample was taken out of vacuum for further analysis by a Bruker D8 Discover XRD system. The system consists of Cu X-ray source (λ = 1.54 Å), high resolution optics with a Ge 2-bounce monochromator and a centric Eulerian cradle with Chi/Phi rotations and X-Y-Z translations. Θ-2θ scans were performed on all the films to examine their bulk crystallization and φ scans were performed on epitaxial films. The system is also capable to do high-resolution XRD, gracing incidence diffraction and reflectometry for thickness calibration.

4.2.6 Substrate preparation

The quality of topological insulator film is significantly influenced by the condition of surface of substrate. The sapphire (c-cut) and STO (111) have hexagonal surface lattices, which makes them the best candidates for depositing topological insulator. The sapphire is a 2inch round wafer, and STO is 2cm by 2cm square wafer. For STO, we usually dice the wafer into 5mm by 5mm, and then use them to deposit topological insulator. The preparation processing of substrates is shown below.

1. Sapphire

The first step to prepare sapphire is to deposit a Nb film on the back side of the wafer. Because sapphire is transparent, and it cannot be heated by electromagnetic waves, we need to deposit Nb on the back side of sapphire. After the sample is loaded into FEL chamber, it will be transferred to E chamber for Nb deposition. When it is transferred from left train to right train, we need to turn the sample upside down. After the sample is transferred into E chamber, we need to wash the gas line: 3 times for rubber tube and 1 time for Argon ring. The parameters for depositing back Nb film are: Manipulator rotation: 15rad/s; Manipulator position 50; Nb 2 position: 20 Throttle:20 degree**.** And the flux of Argon gas is 30sccm/s, the power for sputtering is 70 W. The deposition time is usually 20mins.

After deposition of Back Nb, sapphire wafer will be transferred into G chamber for back-sputtering with Argon ion. This step is to remove the contamination and several atomic layers of sapphire surface, to make sure the surface is completely clean before deposition. When it is transferred from right train to left train, we need to turn the sample upside down. After the sample is transferred into G chamber, we need to strike Argon plasma. First, we need to clean gas line for 5~10 times, and then, we need to adjust pressure to 5E-3mBar. Then we need to strike Argon plasmon at 5E-3mBar pressure for 5 mins.

After the back-sputter, the substrate is needed to anneal in in A chamber to reconstruct the crystal structure of the surface. This step usually takes 9 hours. Before setting the temperature

sequence, make sure the output power is turned on, otherwise, the temperature of substrate cannot be increased.

i. Heat to 500 ℃ in 50 minutes, stay for 1 hour at 500 ℃
ii. Then increase temperature to 800℃ in 50 minutes, stay for 1 hour at 800℃. The surface begins to reconstruct at this temperature.
iii. Heat to 1000 ℃ in 30 minutes, stay for 15mins. This step cannot last too long because the Oxygen atoms of the surface will be depleted at such high temperature.
iv. Decrease to growth temperature and wait for at least 30 minutes for temperature to be stable.

2. STO

To obtain an atomic flat surface, the STO substrate was first etched by 10-1 BOE solution for 3 minutes and rinsed in DI water for 1 minute, then annealed in tube with mixture of 20% oxygen and 80% Ar gas flow at 1000 ^{o}C for 150 minutes.

4.2.7 Deposition of topological insulator

Before the deposition of topological insulator, it is necessary to calibrate fluxes and growth rates by BFM and QCM in advance. A quartz crystal microbalance (QCM) measures a mass variation per unit area by measuring the change in frequency of a quartz crystal resonator. Given the surface area of QCM, the number deposit on the substrate per minutes can be calculated. Figure is the measurement results of deposition rates of Bi, Sb and Te sources. A higher temperature leads to a higher deposition rate. Because it is easy for Te to deposit at the valve of the cracker, its deposition rate has to be calibrated regularly. [38]

However, despite the atomic number from each source can be calculated by the QCM results, the atomic weight of topological insulator cannot be calculated by QCM, because the atoms may not succeed in depositing on the substrate, especially Te atoms. Therefore, after the calibration of sources temperature, the substrate temperature is the major influential factor to the quality of topological insulator. Usually, it is more difficult for Te to deposit with a higher substrate temperature. At 310 ^{o}C, the Te is barely deposit on the substrate. Compared to Te, Sb and Bi have higher volatile point, which makes them easy to deposit.

(a)

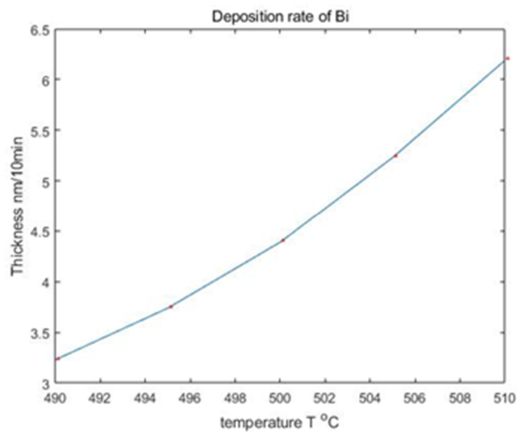

(b)

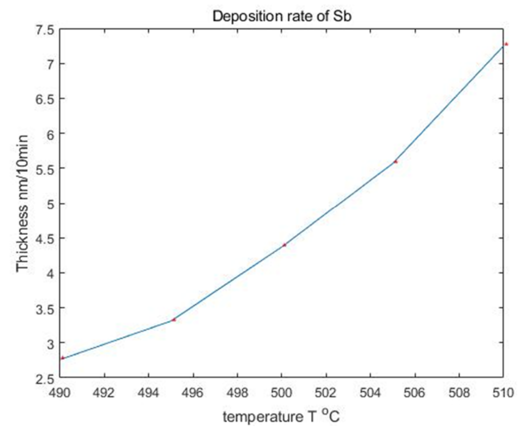

(c)

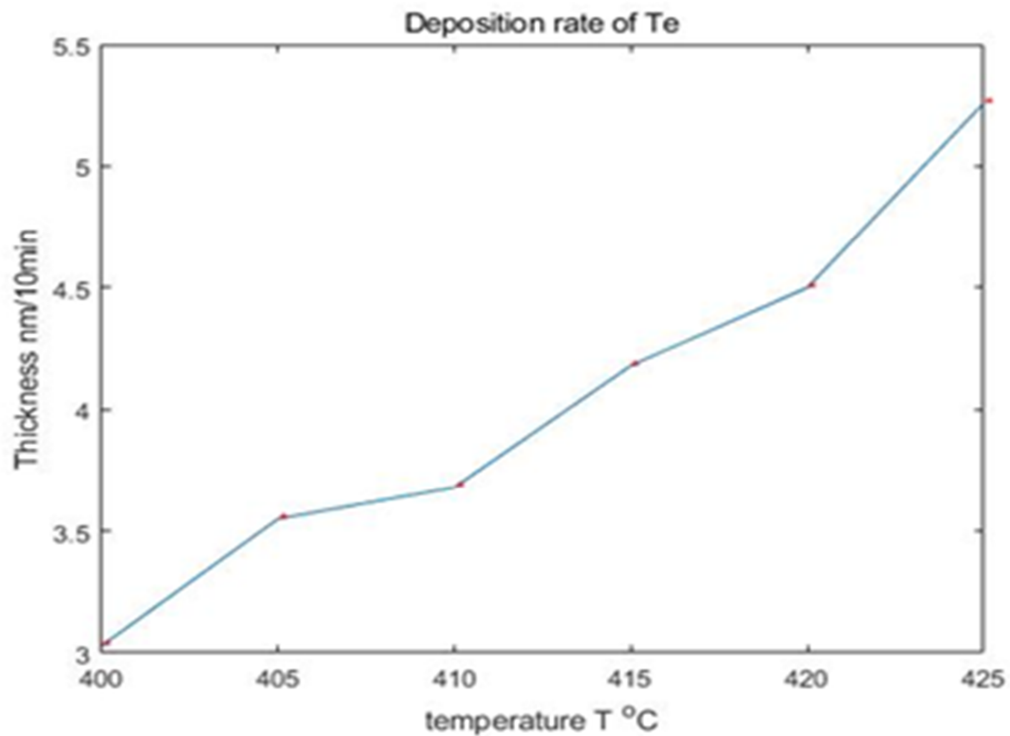

Figure 4-5: (a)deposition rate of Bi, (b) deposition rate of Sb, (c) deposition rate of Te

After the calibration, we should turn on Rheed to observe the status of substrate. The surface of STO (111) is shown in Figure (a). After tuning the Kikuchi lines clear, we can start deposit topological insulator. The Rheed pattern will become dark after the begin of deposition, because

the island growth of topological insulator will increase the surface roughness. (Figure (b)) After one QL is formed, the Rheed pattern will revive. (Figure (c)). Typically, to deposit 10nm $(Bi_{1-x}Sb_x)_2Te_3$ will take 4 mins. Figure (d) is the Rheed pattern $(Bi_{1-x}Sb_x)_2Te_3$, which shows clear crystal direction. The intensity oscillation of Rheed can be used to determine the time for one layer. It usually takes 50sec to deposit one layer of $(Bi_{1-x}Sb_x)_2Te_3$. More oscillation usually means better sample. For undoped BST, the substrate temperature is a major variable. The best substrate temperature is 185 ºC. And the sources temperatures are : Bi:490 ºC, Sb:400 ºC, and Te: 410 ºC.

(a) (b)

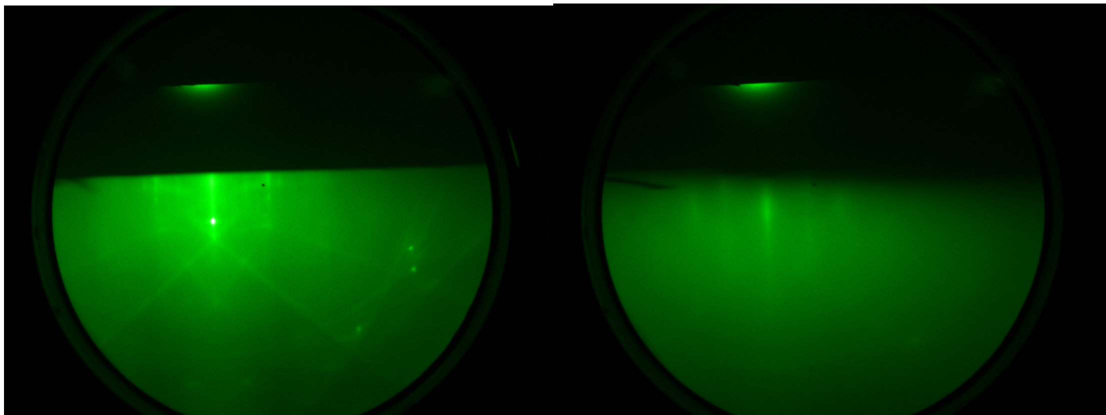

(c) (d)

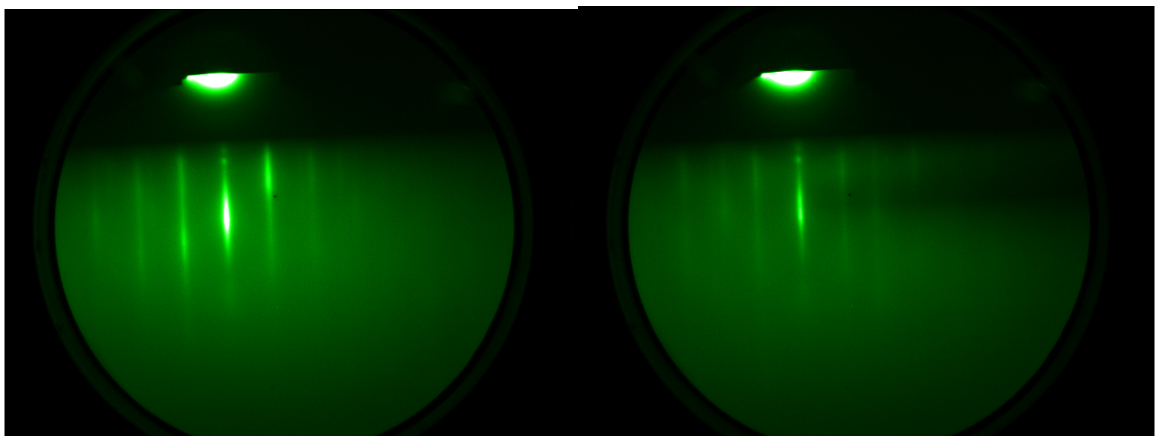

(e)

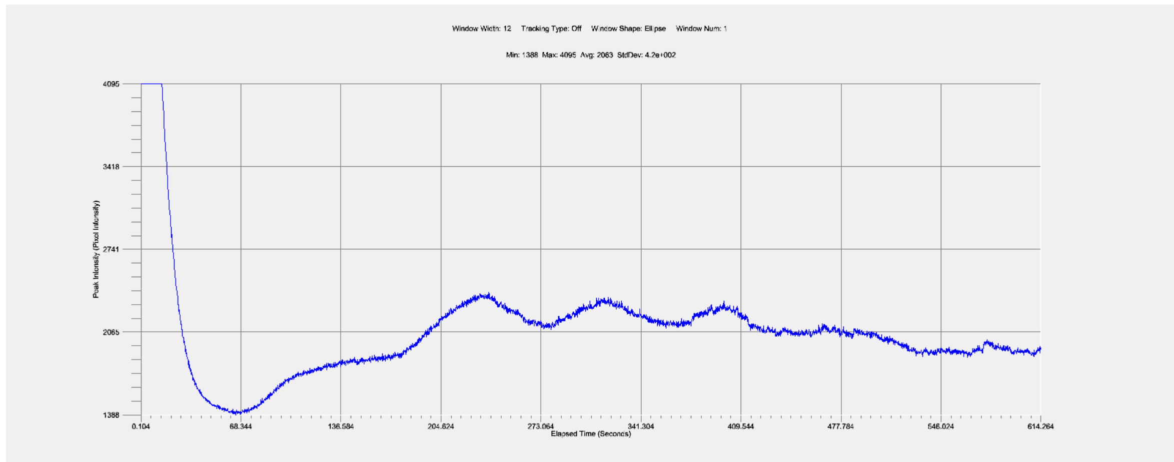

Figure4-6: (a) Rheed pattern for STO (111). (b) Rheed pattern of $(Bi_{1-x}Sb_x)_2Te_3$ after 1mins deposition. The Rheed pattern become dark because of island growth of $(Bi_{1-x}Sb_x)_2Te_3$. (c) after depositing an entire layer, the Rheed pattern becomes clear again. (d) Rheed pattern of $(Bi_{1-x}Sb_x)_2Te_3$ surface. (e) the intensity oscillation of Rheed. One oscillation is corresponding to the growth of one layer.

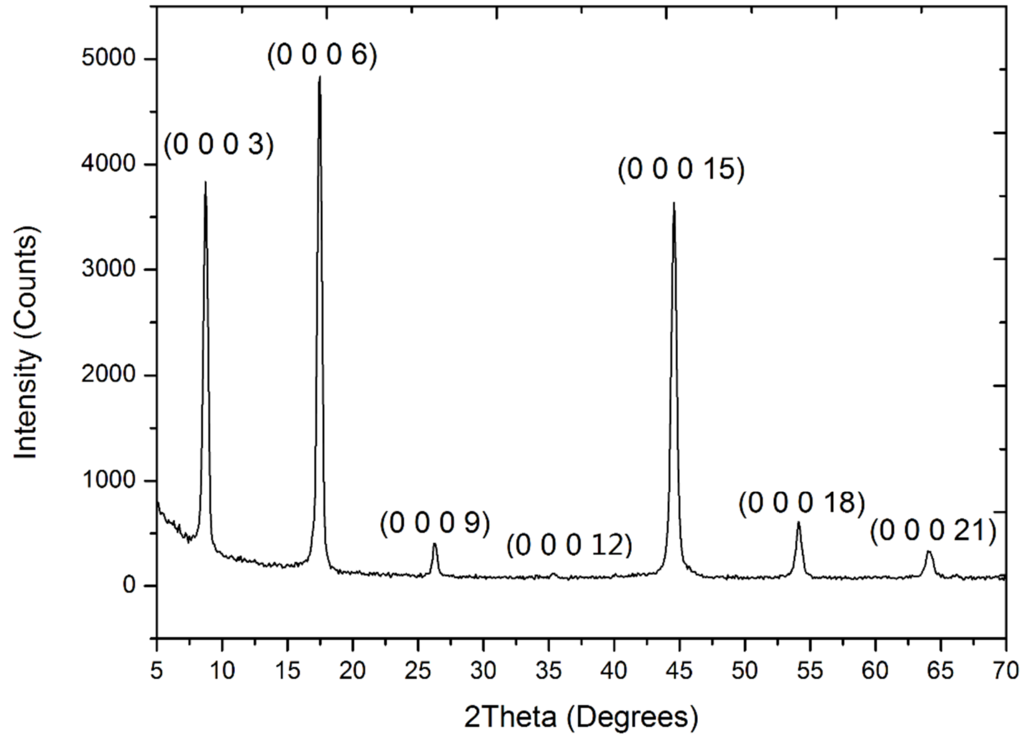

Figure4-7: XRD coupled θ-2θ scan showing peaks from $(Bi_{1-x}Sb_x)_2Te_3$ {0 0 0 1} plane family. Substrate is sapphire.

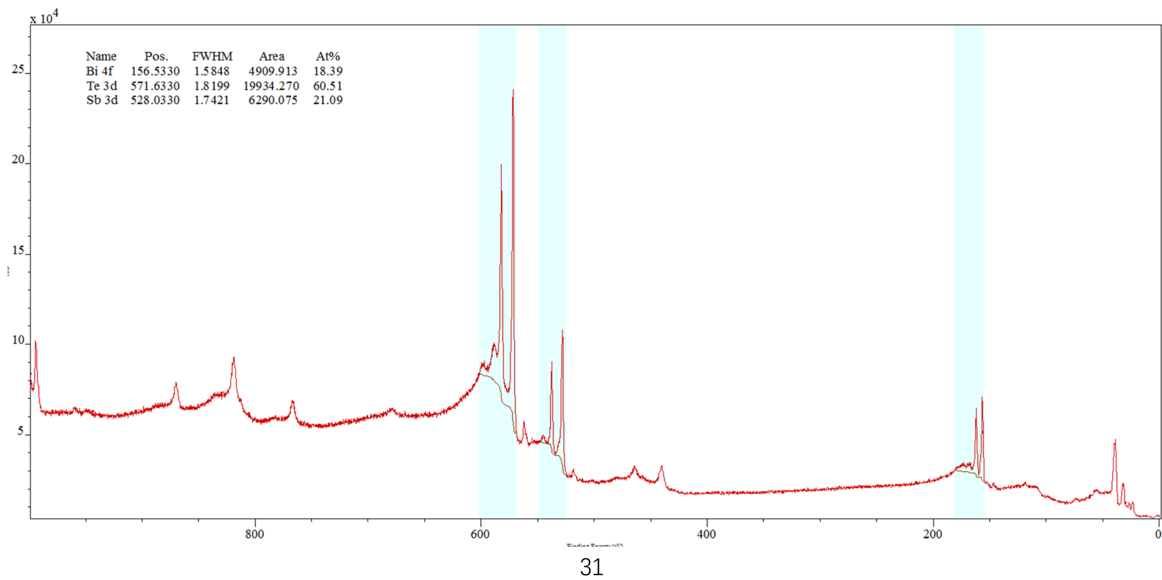

Figure 4-8: XPS measurement with Al – Kα 1486 eV source

Figure 4-7 and Figure 4-8 are the XRD and XPS measurement of $(Bi_{1-x}Sb_x)_2Te_3$ film. The XRD characterize the crystalline quality of bulk $(Bi_{1-x}Sb_x)_2Te_3$ film. Figure 4-7 is the θ-2θ XRD scan $(Bi_{1-x}Sb_x)_2Te_3$ film deposited on sapphire. This result demonstrated that the crystal was c-axis orientated because only the characteristic diffraction peaks from the plane family {0 0 0 1} can be seen. Figure 4-8 is the XPS measurement of $(Bi_{1-x}Sb_x)_2Te_3$ film with Al – Kα 1486 eV source. The position of XPS peaks is exploited to confirm the existence of each element, while the area below each peak is used to calculate the atomic weight of each element. According to the calculation results, the atomic ratio of Bi:Sb:Te is 18:20:60. The quality of topological insulator will be tested by transport menstruant and the feedback will help to optimize deposition conditions.

4.2.8 Deposition of superconductive Nb

In order to fabricate Josephson junction, superconductive Nb has to be deposited on the topological insulator film. Module 8 is the electron beam evaporation chamber, which is equipped with Nb, Au and other magnetic materials. Deposition of superconductive Nb require ultra clean Argon ions to strike Nb sources. The sputtered Nb atoms will deposit on the substrate. Before the deposition, it is required to clean the Argon gas line 5 times to makes sure the Oxygen contamination is as low as possible. After gas line cleaning, we should strike plasma, open the shutter and pre-sputter at 50 W for 30 min. This step is to remove the contaminated layer of Nb source, because even with the shutter closed, there is a chance for other materials to deposit on the surface of Nb source. After pre-sputter, we can turn the power to 200 W to deposit superconductive Nb. At his power, the acceleration voltage of Argon ions is very high, which is another approach to guarantee the purity of deposited Nb. Usually, depositing 100nm Nb will take 4 mins at 200 W. Here are deposition parameters:

Argon ring: 30sccm Power: 200W Time:4min Manipulator rotation: 15rad/s Manipulator position 50 Nb 2 position: 20 Throttle:20 degree

Chapter 5

Nanofabrication processing

5.1 Introduction

The nanofabrication processing includes two major steps: device isolation and junction slit fabrication. The first step is to fabricate Hall bar on the uniform film by optical lithography and reactive ion etching (RIE). The minimum feature of the device is 3um, which meets the optical lithography limit——1um. Then, we exploit RIE to remove the exposed part of optical lithography, because the acceleration voltage of RIE is adjustable, which makes it easier to control etching rate. The second step is to etch a slit on the Hall bar to form a Josephson junction. Since the slit is only around 200nm, we have to use electron beam lithography (EBL), which has higher resolution compared to optical lithography. After EBL exposure, we remove the top Nb layer by RIE with highly selective recipe. Finally, we observe the fabrication results with SEM.

5.2 Optical lithography

Optical lithography or UV lithography is a process used in microfabrication to pattern parts of a thin film or the bulk of a substrate. It uses light to transfer a geometric pattern from a photomask (also called an optical mask) to a photosensitive (that is, light-sensitive) chemical photoresist on the substrate. The wavelength of a lithography aligner determines the minimum size it can expose. For the Maskless Aligner 150, the wavelength of UV source is 405nm, with 1 um minimum exposure feature.

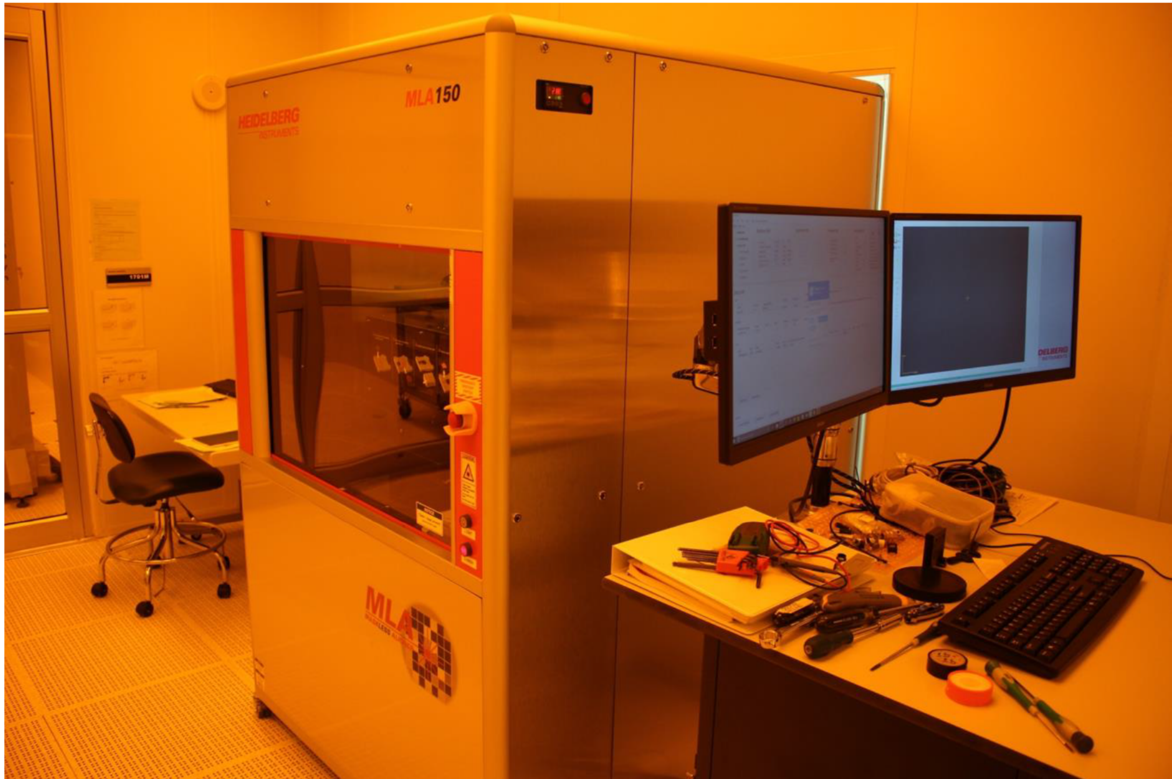

Figure 5-1: MLA 150 UV Maskless Aligner (HEIDELBERG-MLA)

The MLA150 is a high-speed direct write lithography tool capable of exposing photo-sensitive resists. The ability to expose patterns directly without fabrication of a mask, allows for increased design flexibility, and shorter prototyping cycles. The tool is equipped with a pair of diode lasers operating at 405 nm and 375 nm, allowing exposure of a wide range of resist types. Topside and backside cameras allow for alignment to previously patterned features with high accuracy. The stage can accommodate pieces from 8 mm x 8 mm squares up to 9" wafers. The MLA software offers a number of exposure modes, pattern manipulation, and distortion compensation.

The basic steps for optical lithography involve spin-coating, exposure and development. Details are given below:

a) Spin coating recipe for S1805/S1811

Dispense resist with pipette or clean beaker. Then, spread resist at 500RPM for 3---5 seconds ramping up speed at 100RPM/s. Spin resist at 5000 RPM for 60 sec, ramping up speed at 500

RPM/s. This spin speed corresponds to approximately 1400 nm resist thickness (measured by Filmetrics F50---UV). Soft bake: 110degree for 90 sec.

b) Exposure and development

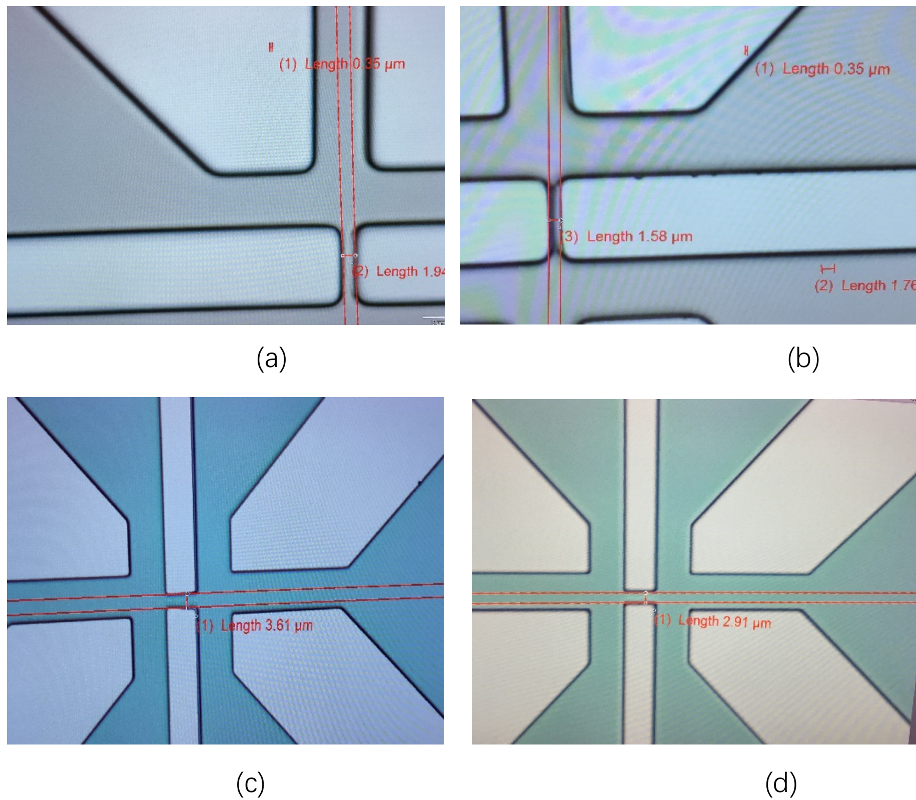

Figure 5-2: Observation of optical lithography results by microscope. (a&b) Overdoes (100[m]/cm^2) for optical lithography. Designed channel width is 4um, while only real width is less than 2um. (c&d) Picture for optical lithography after does test. 0.5um variation is not avoidable for MLA.

After exposure, the wafer is developed in MF-319 for 40 sec, and rinse in DI water for 1 min. S1805/S1811 are positive resist. The exposed area will be removed after development. However, the small feature (~um) may become different from the designed pattern, mostly because of the diffraction limit of laser wave and inappropriate does. Usually, a does test is required before optical lithography. Typical overdoes situation is shown in Figure5 (a&b). Designed width is 4 um,

but exposed width is only 1.6 um. Figure5 (c&d) are exposed feature after a does test. For 4um channel, the exposed width is 3.61 um; for 3um channel, exposed width is 2.91um. For optical lithography, a 0.5um variation from designed width is typical. Here are the parameters: does: 75[m]/cm^2 Defoc:-5

c) PMGI

PMGI is usually used to help lift off photoresist after etching. It should be spin-coated under photoresist. Because it resolves in developer faster than the photoresist, it will leave small gaps along the device edges, these small gaps will make it easier to lift off photoresist. The procedure is i) Dispense resist with pipette or clean beaker, ii) Spread resist at 500RPM for 3---5 seconds ramping up speed at 100RPM/s. Spin resist at 5000 RPM for 60 sec, ramping up speed at 500 RPM/s. iii) Soft bake: 140°C for 90 sec.

5.3 Reactive ion etching (RIE) for device isolation

RIE uses chemically reactive plasma to remove material deposited on wafers. RIE is a type of dry etching which has different characteristics than wet etching. The plasma is generated under low pressure (vacuum) by an electromagnetic field. High-energy ions from the plasma attack the wafer surface and react with it. The chemical reaction of ions and target materials makes RIE highly selective, which means it has quite different etching rate for different materials.

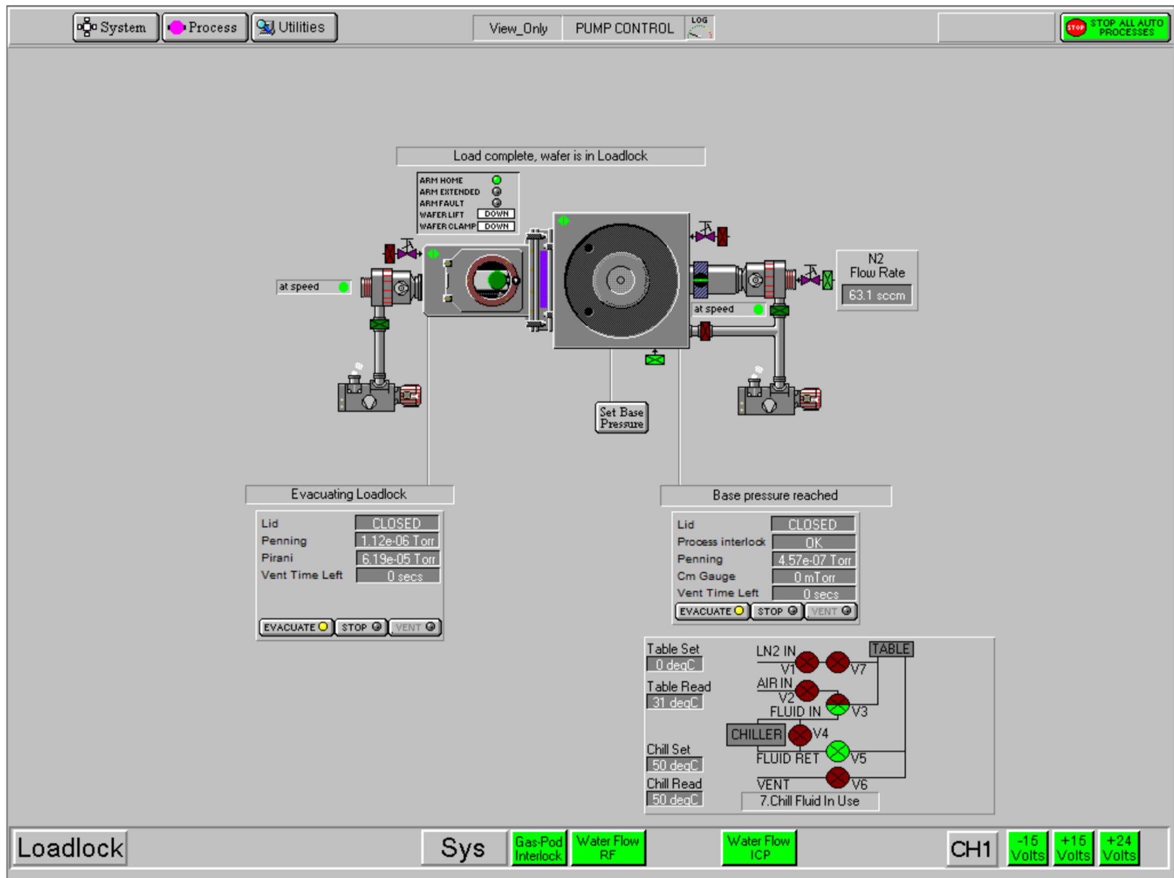

Figure 5-3: Configuration of Oxford PlasmaLab 100 ICP380 Chlorine RIE system

The RIE tool we used is Oxford PlasmaLab 100 ICP380 Chlorine RIE etcher system. It has two major chambers: load-lock chamber and etching chamber. The etching chamber is preserved under -5mbar pressure. It has currently serval recipe available and characterized for the following processes:

- Al RIE/ICP etch
- Cr RIE/ICP etch
- Nb RIE/ICP etch
- Quartz silica etch
- SiNx etch
- SiO2 etch

The processing gases available in the system: Cl2, BCl3, Ar, O2, N2, SF6, C4F8. An automated

pressure controller allows precise control of processing pressure.

There is no need for high-selective recipe for device isolation. So, we only use Argon ions to etch through two layers. As in Figure6(a), the RF power is set to 1200 W, and DC bias power is set to 100 W. For 100nm Nb and 10nm BST, the etching time is 6min 30 sec.

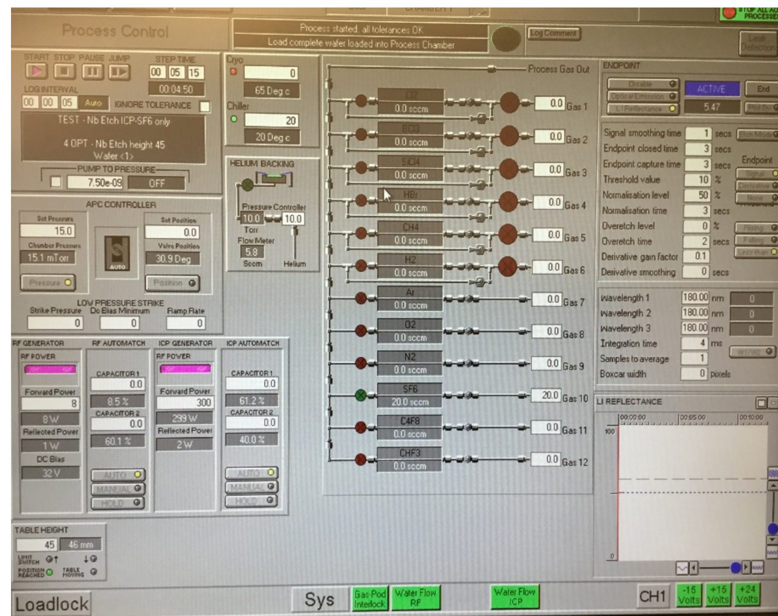

(a)

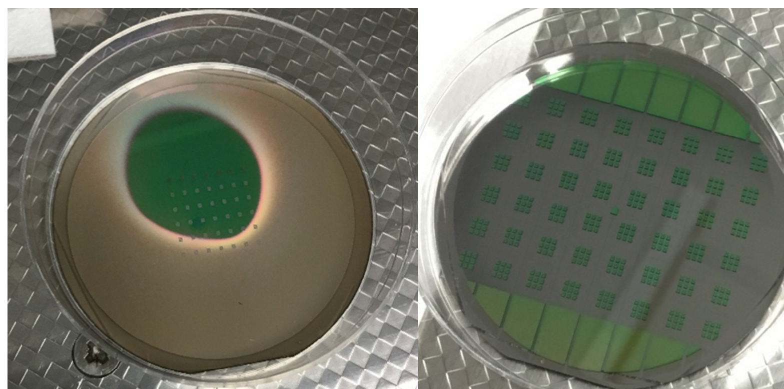

(b) (c)

Figure5-4 (a) RIE parameters for Argon ions recipe. (b) The burned resist on a wafer. (c) A well-etched wafer.

For this recipe, because the plasma keeps heating the sample, the resist may get burned. A

burned resist is shown in Figure6 (b), after the etching, photo resist turns into brown (Carbon), and is not possible to be lifted off by PG remover or acetone. A well-etched wafer is shown in Figure6 (c), we can see the small shadow at the edge of each device because sapphire is transparent, which means both layers are etched through.

After etching, the wafer should be left in PG remover overnight for lift-off.

5.3 Electron beam lithography (EBL)

EBL is the practice of scanning a focused beam of electrons to draw custom shapes on a surface covered with an electron-sensitive film called a resist (exposing). The electron beam changes the solubility of the resist, enabling selective removal of either the exposed or non-exposed regions of the resist by immersing it in a solvent (developing). The minimum feature of a EBL pattern can goes down to the nanometer scale.

The tool we used is JBX-6300FS. Equipped with a thermal field emission electron gun with a ZrO/W emitter, JEOL EBL is an electron beam lithography system provided with the vector scan method for beam deflection. The beam deflection employs 19-bit DAC, and an accelerating voltage of 100kV. The workpiece stage is driven by the step-and repeat-method, and substrates from 5 mm X 5 mm pieces up to 150 mm wafer can be loaded. The operation system of the computer is Linux. The calibration and the exposure are controlled through a graphical user interface (GUI).

Figure 5-5: The JBX-6300FS tools

The basic steps for EBL involve spin-coating, exposure and development. Details are given below:

a) Spin coating recipe for Zep-520

Dispense resist with pipette or clean beaker. Then, spread resist at 500RPM for 3---5 seconds ramping up speed at 100RPM/s. Spin resist at 5000 RPM for 60 sec, ramping up speed at 500 RPM/s. Soft bake: 180degree for 5 minutes.

In case of sapphire or other insulator substrate, a conductive polymer (AR-PC 5090.02) is required because sapphire in not conductive. Spread polymer at 500RPM for 3---5 seconds ramping up speed at 100RPM/s. Spin resist at 2000 RPM for 60 sec, ramping up speed at 500 RPM/s. There is no need to bake after spinning of conductive polymer.

b) EBL

We can also use EBL for device isolation. However, it will take longer time than optical lithography. Usually, under 9nA condition, a 4000um by 400um area will take 2.5 hours to expose. For large feature, the best does is **220uC/cm^2**. (Figure 7a). Typical overdoes situation is shown in Figure7b. The channel is exposed because of the proximity effect and will be removed during development step. Mostly, small features (~10nm) require larger does than large feature (~um). However, for ZEP 520 and conductive polymer, 220uC/cm^2 also works well for the slit fabrication of Josephson Junction.

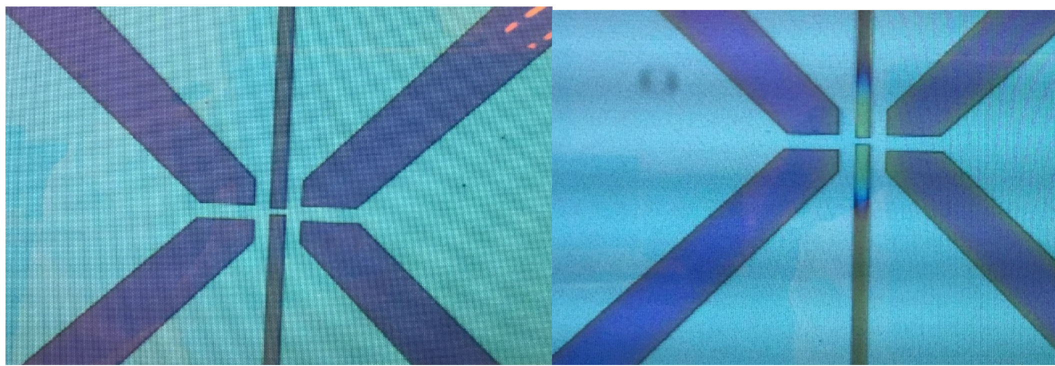

(a) (b)

Figure 5-6: Device isolation results. Observed by microscope. (a)Device isolation result by EBL does 220UC/cm2 (b) Overdoes situation of EBL

5.5 RIE for Josephson Junction

(a) (b)

Figure 5-7: Software interface of RIE system. (a) Etching time of SF6 recipe. Measured by laser end. (b) Parameter settings of RIE recipe for Junction etching

To fabricate Josephson Junction, we need to etch through top Nb layer with protect the bottom BST layer. We set up a RIE recipe that only contain SF6 to chemically etch Nb. The RF power is set to 300 W and DC bias is set to 8 W and it takes 2 min 03 to etch 100nm Nb. Figure8 shows the reflection signal measured by laser end. However, etching rate of large feature (~um) is quite different from that of small feature. (~hundred nm) Therefore, we need to adjust DC bias to acquire an efficient etching result. The DC bias is a vital parameter here, because it is the acceleration bias of ions. The higher is the DC bias, the stronger is the physical etching. And the physical etching may destroy the BST layer. On the contrary, if the DC bias is too low, the cross section of the junction is not steep enough, and the Nb layer is not etched through.

5.6 Fabrication results

Figure 5-8: JSM 7200-F SEM

The JSM 7200-F is a field emission scanning electron microscope, equipped with a Schottky field-emission electron gun, several electron detectors, and versatile imaging software. This combination allows the tool to be used in a number of observation modes to image samples. The Schottky field-emission electron gun can provide beam currents ranging from a few pA up to hundreds of nA. The beam is very stable, eliminating the need for 'flashing' commonly used in cold-cathode field emission sources. The large sample chamber can accommodate substrates ranging in size from a few mm to 4" wafers.

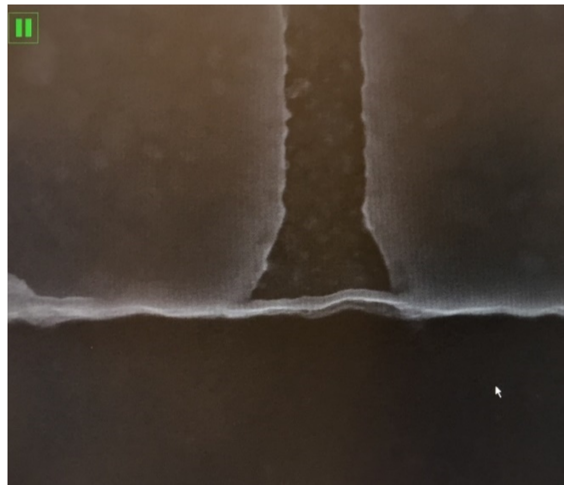

(a)

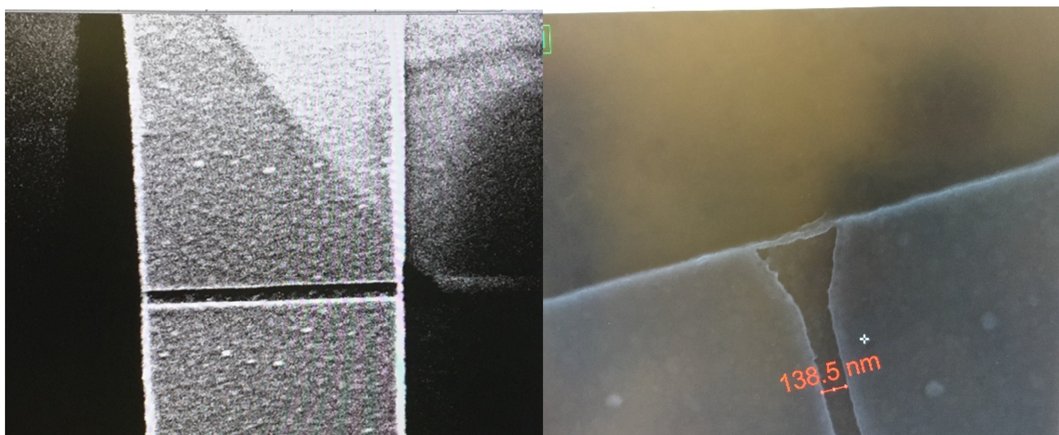

(b) (c)

Figure 5-9: (a&b) SEM picture of Josephson Junction. Re-deposition will result in an extra

channel. (white line connecting two superconducting regions.) (c) The width of junction is 138.5nm.

Figure5-9 are the SEM pictures of Josephson Junction. In Figure (c), the designed width is 120 nm, while real width is 138nm. A re-deposition problem may rise for high DC bias recipe in RIE, which leaves a conductive channel as shown in Figure (a). However, this problem can be avoided by decreasing DC bias in device isolation step. I also conducted an EDX analysis to figure out if the Nb layer is completed etched through.

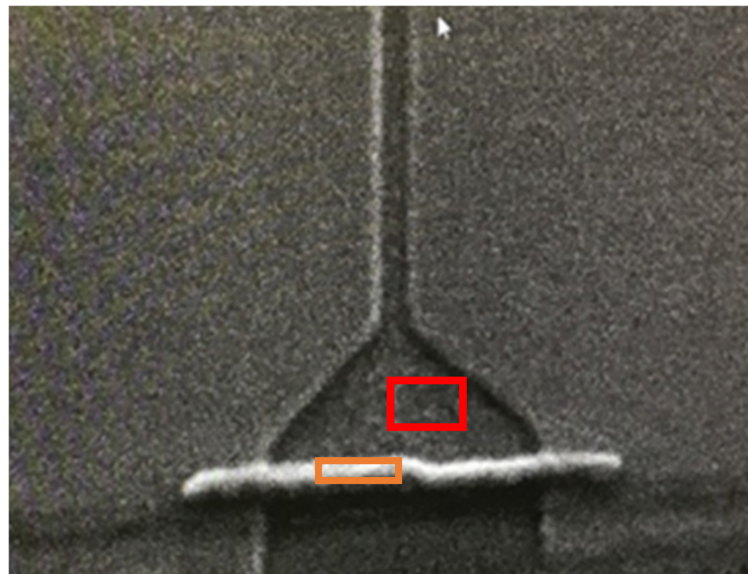

Figure 5-10: SEM picture demonstrating re-deposition problem

	Red area	Orange area
C	13.94	24.43
O	39.41	40.22
Al	43.71	32.24
Nb	2.75	3.10

Table5-1 Atomic weights of red area and orange area in Figure 5-10

. After reducing the EBL does, the junction length varies from 80nm to 120 nm based on the designed width as 40nm to 70nm. However, we can still observe the residue at the edge of the junction. (The red area in Figure 5-10) By the EDX analysis in the red and orange area in Figure5-

10. The atomic weights are shown in table 5-1. The Bi, Sb and Te elements are also detected by EDX. The major different elements of red area and orange are Carbon and Al. The difference of Carbon indicates the residue is mostly photoresist. As for the Al difference, we believe the Niobium under the residue is etched away, so it is not in contact with the substrate. Therefore, the Al has different atomic weights.

Chapter 6

Summary

The chiral Majorana zero modes are predicted to exit at the interface between topological phase and trivial phase in a topological-insulator-based Josephson junction. [1] The edge states of topological insulator are engineered with superconductor proximity effect. Some segments of the edge states are maintained in the topological phase while the rest is not. This setup is demonstrated incapable of conducting braiding and fusion of Majorana fermions. [3] And the existence of Majorana fermions is confirmed by the fractional Josephson effect. Based on these former works, we explored the Andreev bound states of Josephson junctions. Specifically, the achievements are summarized below:

1. **Simulation of Andreev bound states with strong proximity effect.** We explored the behavior of Andreev bound states of a vertical junction, whose proximity effect is strong enough to influence the middle layer. In contrast to common sense, we demonstrated that too strong proximity effect will harm the Majorana modes by opening a gap in the middle layer. The periodicity of Andreev bound states is altered from 4π to 2π, which indicate the tunnelling between Majorana fermions is quenched.

2. **Growth of high-quality topological insulator.** We deposit $(Bi1\text{-}xSbx)_2Te_3$ with MBE and characterize the crystal structure with Rheed and XRD. We optimized the deposition condition and the preparation steps for substrate. Then, exploiting feedback information from XPS and transport measurement, we adjusted sources condition to acquire high-quality topological insulator.

3. **Fabrication of Josephson junction.** We investigated different fabrication methods and developed a fabrication processing for topological-insulator-based Josephson junction.

Exploiting optical lithography, electron beam lithography and reactive ion etching, we fabricated dozens of Josephson junctions. Then we observed the fabrication results by SEM.

The exploration of Majorana modes in condensed matter physics has just begin and will be active for a very long time in the future. Although the existence of Majorana fermions in 1D system has been confirmed, the experimental evidence in 2D Josephson junction is still ambiguous. Moreover, the demonstration of quantum computation with Majorana fermions is still a long way to go. We are convinced that the exploration of Majorana fermions in Josephson junction will lead to more profound understanding of condensed matter physics and provide a promising solution to quantum computation.

Bibliography

[1] Kitaev A Y. Unpaired Majorana fermions in quantum wires. Phys.–Usp. 44 131, 2001

[2] S. Das Sarma, M. Freedman, and C. Nayak, Topologically protected qubits from a possible non-Abelian fractional quantum Hall state. Phys. Rev. Lett., 94, 166802, 2005.

[3] P. Bonderson, M. Freedman, and C. Nayak, Measurement-only topological quantum computation. Phys. Rev. Lett. 101, 010501, 2008.

[4] Fu L and Kane C L, Superconducting proximity effect and Majorana fermions at the surface of a topological insulator, Phys. Rev. Lett. 100 096407, 2008

[5] Fu L and Kane C L, Majorana fermions and a topological phase transition in semiconductor-superconductor heterostructures, Phys. Rev. B 79 161408(R), 2009

[6] Jason Alicea, New directions in the pursuit of Majorana fermions in solid state systems. Rep. Prog. Phys. 75, 076501, 2012

[7] L Jiang, D Pekker, J Alicea, G Refael, et. al. Unconventional Josephson signatures of Majorana bound states, Phys. Rev. Lett. 107, 177002, 2011

[8] M Snelder, M Veldhorst, AA Golubov, A Brinkman, Andreev bound states and current-phase relations in three-dimensional topological insulators. Phys. Rev. B. 87, 104507, 2013

[9] RR Schaller, Moore's law: past, present and future, IEEE spectrum,34,6, 1997

[10] Chetan Nayak, Steven H. Simon, Ady Stern, Michael Freedman, and Sankar Das Sarma, Non-Abelian anyons and topological quantum computation, Rev. Mod. Phys. 80, 1083, 2008

[11] Wilczek, F. Fractional Statistics and Anyon Superconductivity, World Scientific, 1990

[12] Gangadharaiah S, Braunecker B, Simon P and Loss D, Majorana edge states in interacting one-dimensional systems, Phys. Rev. Lett. 107 036801, 2011

[13] Sela E, Altland A and Rosch A, Majorana fermions in strongly interacting helical liquids, Phys. Rev. B 84 085114, 2011

[14] Sau J D, Tewari S, Lutchyn R M, Stanescu T D and Das Sarma S, Signatures of Majorana fermions in hybrid superconductor-semiconductor nanowire devices, Phys. Rev. B 82 214509, 2010

[15] Romito A, Alicea J, Refael G and von Oppen F, Manipulating Majorana fermions using supercurrents, Phys. Rev. B 85 020502, 2012

[16] Xiao D, Zhu W, Ran Y, Nagaosa N and Okamoto S, Interface engineering of quantum Hall effects in digital transition metal oxide heterostructures, Nature Commun. 2 596, 2011

[17] Potter A C and Lee P A, Engineering a p+ip superconductor: Comparison of topological insulator and Rashba spin-orbit-coupled materials, Phys. Rev. B 83 184520, 2011

[18] Kane C L and Mele E J, Quantum spin Hall effect in graphene Phys. Rev. Lett. 95 226801, 2005

[19] Read N and Green D, Paired states of fermions in two dimensions with breaking of parity and time-reversal symmetries and the fractional quantum Hall effect, Phys. Rev. B 61 10267, 2000

[20] DI Pikulin, YV Nazarov, Phenomenology and dynamics of a Majorana Josephson junction - Physical Review B,86, 140504(R), 2012

[21] van Heck B, Hassler F, Akhmerov A R and Beenakker C W J, Coulomb stability of the 4π

-periodic Josephson effect of Majorana fermions, Phys. Rev. B 84 180502, 2011
[22] Badiane D M, Houzet M and Meyer J S, Unconventional Josephson signatures of Majorana bound states, Phys. Rev. Lett. 107,177002, 2011
[23] P San-Jose, E Prada, R Aguado, AC Josephson effect in finite-length nanowire junctions with Majorana modes, Phys. Rev. Lett. 108,257001, 2012
[24] Jiang L, Pekker D, Alicea J, Refael G, Oreg Y and von Oppen F, Unconventional Josephson signatures of Majorana bound states, Phys. Rev. Lett. 107,236401, 2011
[25] Kwon H-J, Sengupta K and Yakovenko V M, Fractional ac Josephson effect in p-and d-wave superconductors Eur. Phys. J. B 37 349, 2004
[26] Kwon H-J, Yakovenko V M and Sengupta K, Fractional ac Josephson effect in unconventional superconductors Low Temp. Phys. 30 613, 2004
[27] Black-Schaffer A M and Linder J, Majorana fermions in spin-orbit-coupled ferromagnetic Josephson junctions, Phys. Rev. B 84 180509, 2011
[28] Meyer, Driss M. Badiane, and Leonid I. Glazman, Dynamics of Majorana States in a Topological Josephson Junction Manuel Houzet, Julia S. Phys. Rev. Lett. 111, 046401, 2013
[29] H. Zhang, C.-X. Liu, X.-L. Qi, X. Dai, Z. Fang, and S.-C. Zhang, "Topological insulators in Bi 2 Se 3, Bi 2 Te 3 and Sb 2 Te 3 with a single Dirac cone on the surface," Nature physics, vol. 5, p. 438, 2009.
[30] Y. Chen, J. G. Analytis, J.-H. Chu, Z. Liu, S.-K. Mo, X.-L. Qi, et al., "Experimental realization of a three-dimensional topological insulator, Bi2Te3," science, vol. 325, pp. 178-181, 2009.
[31] Y. Xia, D. Qian, D. Hsieh, L. Wray, A. Pal, H. Lin, et al., "Observation of a large-gap topological-insulator class with a single Dirac cone on the surface," Nature physics, vol. 5, p. 398, 2009.
[32] D. Hsieh, Y. Xia, D. Qian, L. Wray, F. Meier, J. Dil, et al., "Observation of time-reversal-protected single-Dirac-cone topological-insulator states in Bi 2 Te 3 and Sb 2 Te 3," Physical review letters, vol. 103, p. 146401, 2009.
[33] J. Zhang, C.-Z. Chang, Z. Zhang, J. Wen, X. Feng, K. Li, et al., "Band structure engineering in $(Bi_{1-x}Sb_x)_2Te_3$ ternary topological insulators," Nature communications, vol. 2, p. 574, 2011.
[34] D. Kong, Y. Chen, J. J. Cha, Q. Zhang, J. G. Analytis, K. Lai, et al., "Ambipolar field effect in the ternary topological insulator $(Bi_{1-x}Sb_x)_2Te_3$ by composition tuning," Nat Nanotechnol, vol. 6, pp. 705-9, Oct 2 2011
[35] X. He, T. Guan, X. Wang, B. Feng, P. Cheng, L. Chen, et al., "Highly tunable electron transport in epitaxial topological insulator $(Bi_{1-x}Sb_x)_2Te_3$ thin films," Applied Physics Letters, vol. 101, p. 123111, 2012.
[36] J. Klein, "Epitaktische Heterostrukturen aus dotierten Manganaten," Universität zu Köln, 2001.
[37] A. C. Ichimiya, Philip I., Reflection High-Energy Electron Diffraction. Cambridge, UK: Cambridge University Press, 2004.
[38] F. Yang, Y. Ding, F. Qu, J. Shen, J. Chen, Z. Wei, et al., "Proximity effect at superconducting

Sn-Bi 2 Se 3 interface," Physical Review B, vol. 85, p. 104508, 2012